

## 6 Results from Particle-Resolved Simulations\*

Agathe Chouippe<sup>1</sup>, Aman G. Kidanemariam<sup>2</sup>, Jos Derksen<sup>3</sup>, Anthony Wachs<sup>4,5</sup>, Markus Uhlmann<sup>6</sup>

<sup>1</sup> Université de Strasbourg, Institut ICube, Fluid Mechanics Group, 2, rue Boussingault, 67000 Strasbourg, France

<sup>2</sup> The University of Melbourne, Department of Mechanical Engineering, Victoria 3010, Australia

<sup>3</sup> University of Aberdeen, School of Engineering, King's College, Aberdeen AB24 3UE, United Kingdom

<sup>4</sup> University of British Columbia, Department of Mathematics, 1984 Mathematics Road, Vancouver BC V6T 1Z2, CANADA

<sup>5</sup> University of British Columbia, Department of Chemical and Biological Engineering, 2360 East Mall, Vancouver BC V6T 1Z3, Canada

<sup>6</sup> Karlsruhe Institute of Technology, Institute for Hydromechanics, Kaiserstr. 12, 76131 Karlsruhe, Germany

**Abstract:** We review some of the results obtained to date with the aid of the PR-DNS approach to turbulent particulate flows. It is shown that the method has matured to a point which allows to apply it successfully to a wide variety of fluid/particle configurations, albeit still at a relatively large computational cost. Due to the availability of high-fidelity space-and-time-resolved data, a number of challenging open questions have already been addressed in unprecedented detail.

### 6.1 Introduction

Since its emergence in the late 1990s the method of particle-resolved direct numerical simulation (PR-DNS) has established itself as an eminently useful source of high-fidelity data on turbulent particulate flow. In the PR-DNS approach the Navier-Stokes equations for the fluid flow are solved together with the Newton-Euler equations for rigid body motion (cf. chapter 5) without further modelling assumptions – except for those which relate to solid-solid contacts, cf. chapter 7. Results obtained with this method thereby provide insight into the micro-scale flow around each particle, and on the way these scales couple back to the remainder of the spectrum.

Despite the formidable computational requirements inherent in the PR-DNS approach, a growing body of literature involving such numerical studies has been published over the last two decades. The results have already had a significant impact on the state of the art in particulate flow: (i) they have

---

\*Published as Chapter 6 in *Modeling Approaches and Computational Methods for Particle-laden Turbulent Flows*, S. Subramaniam and S. Balachandar (editors), Academic press, 2022, <https://doi.org/10.1016/B978-0-32-390133-8.00013-X>.

helped to clarify the mechanisms behind various physical phenomena, and (ii) they have aided in the design and validation of simplified models (e.g. of Euler-Lagrange or Euler-Euler type). It is the purpose of the present chapter to provide an overview of the capabilities and current limitations of the PR-DNS approach. Many of the topics touched upon in the following will be picked up in subsequent chapters of the present volume, such as chapter 9 on extended point particle models and chapter 14 on the modelling of fluidized beds.

Since the relevant parameter space is large (particle volume fraction, Galileo number, density ratio, length scale ratio) and particulate flow applications are highly diverse (laminar vs. turbulent background flow, homogeneous vs. inhomogeneous systems, wall-bounded vs. unbounded, fixed vs. mobile particles, turbulence forcing method), the following review can only cover a small subset of this vast topic. Here we have chosen to focus on three aspects. First, in section 6.2 we will give an account of how PR-DNS can be used for the purpose of improving models for quasi-steady drag and for the analogous scalar transfer. Section 6.3 is dedicated to fluid-mediated particle dynamics in dilute unbounded flow with and without a priori turbulence. Finally, we turn our attention to wall-bounded shear flow in section 6.4, where we discuss vertical and horizontal channel flow, the latter one in the absence or presence of a thick sediment bed, possibly featuring macroscopic patterns.

## **6.2 PR-DNS of dense fluidized systems for drag force parameterizations based on dynamic simulations**

Particle-resolved simulations of suspensions in triple periodic domains have been performed to probe solids-fluid and solids-solids momentum transfer and – more generally – the evolution of the microstructure of suspensions. In this section, we will restrict ourselves to systems comprised of a Newtonian fluid and solid particles all having the same size. This restriction is for brevity mostly. Simulations with spherical particles having a size distribution as well as simulations with non-Newtonian fluids have been reported [133, 22]. The essentials of their setup and interpretation can be understood in the context of what is described in this section. Particle-resolved simulations involving non-spherical particles are a strongly emerging field of study and Chapter 7 is largely dedicated to simulation methodologies for this subject. At the end of this section we will briefly return to the topic of non-spherical particles.

A number of distinctions for the already quite specific flow configurations still need to be made.

In the simplest configuration, the particles are kept at fixed locations and fluid flows through the particle assemblies under the influence of a constant and uniform body force. Such simulations date back to Ladd [74]. Their most relevant application is in probing fluid-particle drag on spheres as a function of the particle volume fraction, the topology of the particle arrangement (ordered versus random assemblies), and a particle-based Reynolds number. The availability of analytical results for drag on various types of regular static assemblies of spheres at low Reynolds numbers [112, 51] greatly facilitates the verification of the numerical approaches.

Drag in static particle assemblies has practical implications in gas-solid flows, i.e. flows with high Stokes numbers. Then, the time scales over which the particle configurations evolve are much larger than fluid flow time scales at the particle-level (e.g. particle size over superficial velocity) so that a frozen-particle approach is justified. At lower Stokes numbers (e.g. liquid-solid flows) particle configurations respond more directly to flow conditions which – as we will see – has consequences for the drag force.

For specific numerical methodologies as well as results of flow through static particle assemblies – including drag force correlations derived from simulations – we refer to the chapter on fluidization

(Chapter 14) in this book.

In this section the focus is on simulations of freely moving, colliding and rotating spheres in fluid and the information that can be extracted from such simulations. In these systems, agitation can be done in different ways. **(1)** As a direct and logical extension of flows through static solids assemblies, a uniform and constant body force is applied to the fluid. Since the fully periodic system needs to be overall force-balanced, an opposing force is applied to the particles. This usually is interpreted as a fluidized system with the particles feeling gravity and the interstitial fluid pushed through by the body force in the opposite direction [24]. **(2)** By creating turbulence in fully periodic domains, one is able to directly study particle-turbulence interactions. Creating single-phase turbulence can be done through forcing [3]. Placing particles in fully developed single-phase turbulence and letting the system decay enabled Lucci et al [80] to highlight finite particle size effects – specifically for spheres with a diameter larger than the Kolmogorov scale – on the evolution of turbulent kinetic energy (see Chapter 3). Dynamically steady turbulent solid-liquid systems [125] with resolved particles show turbulence modulation consisting of the transfer of turbulent kinetic energy from large scales to length scales of the order of the particle size.

In this section we will provide more detail and results regarding fluidized dynamic systems with solid over fluid density ratios characteristic of liquid fluidization. Full numerical details can be found in [24]. The fluid has density  $\rho_f$  and kinematic viscosity  $\nu$ ; the particles are solid spheres all having diameter  $d_p$  and density  $\rho_p$ . The particle volume fraction is  $\phi$ . This allows to define a mixture density as  $\rho_m = \phi\rho_p + (1 - \phi)\rho_f$ . Gravitational acceleration  $\mathbf{g}$  points in the negative  $z$ -direction of a Cartesian coordinate system:  $\mathbf{g} = -g\mathbf{e}_z$ . The above definitions give rise to a set of three dimensionless input parameters governing the system. Here we select  $\phi$ , density ratio  $\rho_p/\rho_f$  and a Galileo number  $Ga = ((\rho_p/\rho_f - 1)d_pg)^{1/2}d_p/\nu$  as the input parameters.

Each particle experiences a net gravity force  $\mathbf{F}_g = -(\rho_p - \rho_m)\frac{\pi}{6}d_p^3g\mathbf{e}_z$ . An overall force balance then requires a body force acting on the fluid  $\mathbf{f} = (\rho_m - \rho_f)g\mathbf{e}_z$ . In addition to gravity, the particles feel hydrodynamic forces and forces due to close-range particle-particle interactions: radial lubrication and a spring-type force to deal with solid-solid contact (“soft” collisions, Chapter 7 in this book).

As an alternative for soft collisions, a hard-sphere collision algorithm can be implemented [24]. This has the advantage of particles not overlapping so that overall particle volume fraction levels are not being compromised. For dense suspensions ( $\phi \geq 0.4$ ) and/or systems containing many particles ( $N \geq 10^4$ ), hard-sphere collision algorithms slow down the computations significantly given that each collision needs to be accounted for explicitly and that parallelization of the algorithm requires significant communication. No strong sensitivity of simulation results with respect to collision parameters (restitution and friction coefficients) has been observed for solid-liquid flow [24]. This is because most dissipation between approaching particles takes place in the liquid prior to collision, either in the resolved flow or as a result of lubrication modelling.

Simulations are initialized by randomly placing the equally sized spheres in the fully periodic, three-dimensional domain in a non-overlapping manner. There is a limit to the particle volume fraction that can be achieved this way:  $\phi \leq 0.3$  [127]. Higher particle volume fractions can be achieved by a compaction process: first build a random particle configuration with  $\phi < 0.3$  and then let the particles freely move and collide under the influence of a force that attracts them to a centre plane of the domain. Once a desired volume fraction has been achieved, the parts of the volume void of particles are discarded. Alternatively, high particle volume fractions can be generated by “growing” the particles: create an initial non-overlapping random set of spheres with  $\phi < 0.3$ ; give them random velocities and let them move and collide as a granular gas. Each time step one determines the minimum distance  $\delta_{min}$  between two particle surfaces in the entire domain and then increases the radius of

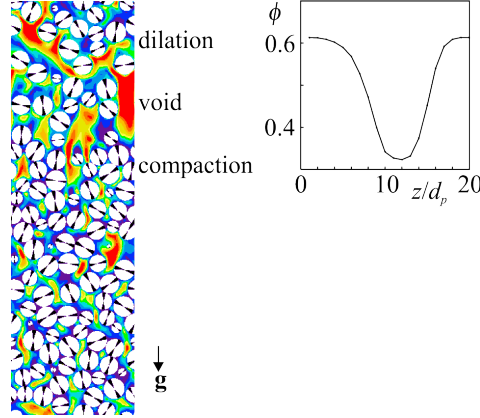


Figure 6.1: Wave instability in liquid fluidized bed [24]. Overall particle volume fraction  $\langle\phi\rangle = 0.51$ ,  $\rho_p/\rho_f = 4.4$  and  $Ga = 133$ . Left: cross section of an instantaneous realization with liquid coloured by velocity magnitude; right: average wave form.

each sphere by an amount slightly smaller than  $\delta_{min}/2$ . This way particle volume fractions up to those associated to random close packing ( $\phi \approx 0.62$ ) can be accomplished.

After initializing the two-phase system, the forces on fluid and solids are activated and we let the system evolve to a dynamically steady state. Under certain conditions and – most importantly – with a sufficiently large domain, wave and void-type instabilities develop [30]. In sufficiently narrow domains, the characteristics of one-dimensional waves (their speed  $c$  and wave form) have been used as a way of validating simulation results with available experimental data [24]. Figure 6.1 shows an impression of a simulation after having developed a planar wave. The dimensionless wave speed  $\tilde{c} = cd_p/\nu$  in experiment [30] and simulation [24] under the conditions (in dimensionless terms) as given in the caption of Figure 6.1 are  $\tilde{c} = 29 \pm 1$  and  $\tilde{c} = 33 \pm 2$  respectively.

Interpretation of simulations in terms of average drag requires determining the average interstitial fluid and solids speed (averaging over volume and time),  $\langle\mathbf{u}\rangle$  and  $\langle\mathbf{u}_p\rangle$  respectively. The superficial slip velocity then is  $(1 - \phi) \left| \langle\mathbf{u}\rangle - \langle\mathbf{u}_p\rangle \right|$  which defines a Reynolds number as  $Re = (1 - \phi) \left| \langle\mathbf{u}\rangle - \langle\mathbf{u}_p\rangle \right| d_p/\nu$ . With a constant net gravity force acting on each particle and – on average – balanced forces on each particle the hydrodynamic force per particle is  $-\mathbf{F}_g$ . This then allows for the definition of a dimensionless hydrodynamic force coefficient as  $F = \frac{(\rho_p - \rho_m) \frac{\pi}{6} d_p^3 g}{3\pi d_p \nu \rho_f (1 - \phi) |\langle\mathbf{u}\rangle - \langle\mathbf{u}_p\rangle|}$  which is the drag force normalized by Stokes drag based on the superficial slip speed.

From a physics perspective, the average dimensionless drag in a homogeneous system ( $F$ ) depends on  $Re$ ,  $\phi$  and the density ratio  $\rho_p/\rho_f$ . Instead of the density ratio, the Stokes number is regularly used as an independent dimensionless variable:  $St = \frac{1}{18} \frac{\rho_p}{\rho_f} Re$ , so that  $F(Re, \phi, St)$ . From a numerical perspective one also needs to consider effects of domain size, spatial (grid) resolution and time step.

As noted above, there is extensive literature on  $F(Re, \phi, St \rightarrow \infty)$  based on PR-DNS's of flow through fixed particle assemblies. The relevance of the Stokes number has been identified in [110] where it is noted that over the full range of particle volume fractions of random assemblies ( $0 < \phi \leq 0.62$ ), and in the low Reynolds number limit, the dimensionless drag force according to fixed-particle simulations by Van der Hoef et al [133]  $F = \frac{10\phi}{1-\phi} + (1 - \phi)^3 (1 + 1.5\phi^{1/2})$  is higher than the empirical correlation by Wen and Yu [143]  $F = (1 - \phi)^{-2.65}$ . The latter correlation is based on liquid fluidization experiments at moderate Stokes numbers. The moderate solids inertia allows the particles to quickly adapt their linear and angular velocity and location such that flow resistance gets reduced as confirmed



by Rubinstein et al [110]. By performing PR-DNS of freely moving spherical particles in periodic domains over a range of density ratios, they quantified – by fitting average drag results of dynamic PR-DNS’s – the way the transition between high and low Stokes number occurs:

$$F = \alpha(\tilde{St}) F_{hiSt} + [1 - \alpha(\tilde{St})] F_{WY}, \quad (6.1)$$

with  $F_{hiSt}$  the high-Stokes limit for which [110] took the Van der Hoef et al [133] correlation,  $F_{WY}$  the Wen and Yu [143] correlation and

$$\alpha(\tilde{St}) = \frac{1}{2} \left( 1 + \frac{\tilde{St} - 10}{\tilde{St} + 10} \right), \quad (6.2)$$

with  $\tilde{St} = \frac{St}{(1-\phi)^2}$ . An extension towards moderate Reynolds numbers (up to 100) of the effect of solids inertia through the density ratio on particle drag has been presented in a comprehensive study by Tavanashad et al [123] based on particle resolved simulations. Drag force correlations play an important role in Euler-Lagrange simulations, see Chapter 13.

Clustering and preferential relative particle locations at moderate Stokes numbers not only have consequences for the drag force, it also impacts mass transfer. This is relevant with a view to the application of suspensions in (chemical) engineering processes to achieve mass transfer between a fluid and a solids phase.

This has been investigated in [23] where – in the same way as discussed above – the joint dynamics of fluid and solids in fully periodic domains driven by a uniform body force has been investigated. Once the solid-fluid system is fully developed one starts solving a convection diffusion equation

$$\frac{\partial c}{\partial t} + \mathbf{u} \cdot \nabla c = \Gamma \nabla^2 c, \quad (6.3)$$

in a passive scalar in the fluid with dimensionless concentration  $c$  having a diffusion coefficient  $\Gamma$ . At moment  $t = 0$ ,  $c = 0$  everywhere in the fluid while  $c = 1$  is maintained at the fluid-solid interface. This way, scalar is transferred to the fluid: for each particle  $i$  at a rate  $\dot{m}_i = -\Gamma \int_{A_i} \partial c / \partial n dA$  with  $A_i$  the surface of the particle and  $n$  the particle-outward normal. The transfer process is parameterized through a transfer coefficient  $k_i$  according to  $\dot{m}_i = k_i S \Delta c$  with  $S = \pi d_p^2$  and  $\Delta c$  a “characteristic” concentration difference (specified below). The Sherwood number is defined as  $Sh_i = k_i d_p / \Gamma$  and (finally) the average Sherwood number is the average over all  $N$  particles in the domain  $Sh = \frac{1}{N} \sum_{i=1}^N Sh_i$ .

This average Sherwood number depends on time with  $Sh \rightarrow \infty$  at  $t = 0$  when scalar penetrates rapidly into fresh fluid. If, however, we define  $\Delta c = 1 - \langle c \rangle$  with  $\langle c \rangle$  the (time dependent) fluid volume-average concentration,  $Sh$  is approximately constant over a wide time window [23]; this constant value we denote as  $\overline{Sh}$ . It now is interesting to note that  $\overline{Sh}$  depends on the solids over liquid density ratio  $\rho_p/\rho_f$ , see Figure 6.2 with  $\overline{Sh}$  increasing with increasing  $\rho_p/\rho_f$  and reaching a plateau if  $\rho_p/\rho_f \approx 10^3$ . The plateau value is approximately equal to  $\overline{Sh}$  obtained from a fixed-particle simulation.

Figure 6.2 also shows drag force data as a function of  $\rho_p/\rho_f$  and we see that the transition of  $F$  occurs in the same density ratio range as  $\overline{Sh}$  lending credit to the hypothesis that clustering in moderate Stokes number suspensions leads to a reduction in mass transfer.

We now briefly turn to the topic of non-spherical particles. To the best of the authors’ knowledge, the problem of fluidization of many non-spherical particles computed with PR-DNS has not been considered in the literature with any other shape than finite-size rods in [27]. Among other things, [27] shows – next to preferential concentration – also preferential orientation and the way it depends

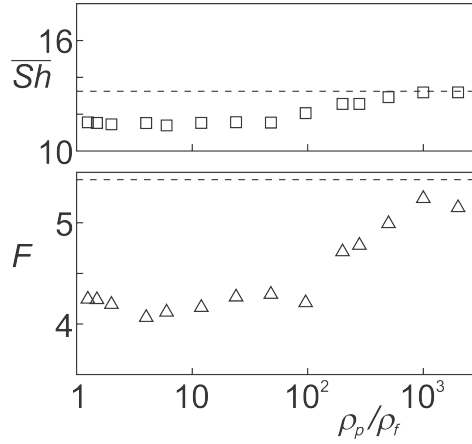


Figure 6.2: Average Sherwood number  $\overline{Sh}$  (top) and drag  $F$  (bottom) as a function of density ratio  $\rho_p/\rho_f$  in a fully periodic domain with freely moving particles with overall particle volume fraction  $\langle\phi\rangle=0.2$  and Schmidt number  $Sc = \nu/\Gamma = 300$ . Dashed lines indicate results of a fixed-particle simulation.

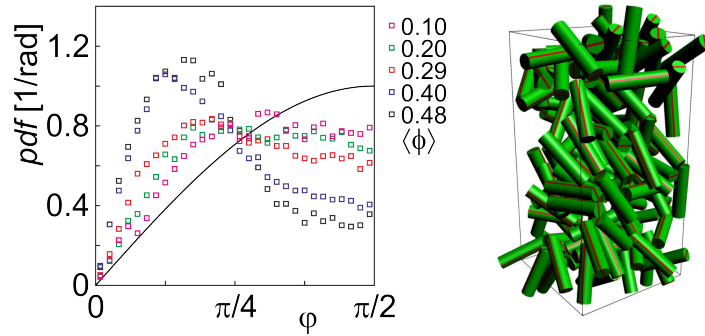


Figure 6.3: Left: orientation distribution of fluidized cylinders with aspect ratio  $\ell/d=4$  in terms of their angle  $\varphi$  with the vertical for a range of overall particle volume fractions  $\langle\phi\rangle$  as indicated. The drawn  $\sin\varphi$  curve is an isotropic orientation distribution. Right: an impression for  $\langle\phi\rangle=0.29$ . Density ratio  $\rho_p/\rho_f=2$  and  $Ga=29$  [27].

on the particle volume fraction  $\phi$  and the length over diameter ratio  $\ell/d$  of the cylinders. Figure 6.3 shows a sample result for  $\ell/d=4$  in terms of the distribution of the angles  $\varphi$  of the fluidized cylinders with the vertical. A fully isotropic orientation distribution implies a distribution of  $\varphi$  according to  $\sin\varphi$ . For  $\phi \leq 0.29$  the orientation distribution is approximately isotropic. For  $\phi \geq 0.40$  the cylinders have a clear preference for small angles  $\varphi$ .

The above results were all obtained through lattice-Boltzmann simulations (see Chapter 5) with an immersed boundary method for achieving no-slip at the solid-liquid interfaces.

Contributions of Euler-Lagrange simulations of fluidization with non-spherical particles are more numerous [135, 46] as compared to particle-resolved simulations. More generally, the complementary problem to fluidization, the free settling of non-spherical particles, has not been examined much with PR-DNS either, [119] with cubes and [38, 42] with spheroids being a few exceptions. Instead, researchers have addressed other, presumably simpler, problems as preliminary steps to pave the way to the full PR-DNS of freely settling or fluidized non-spherical particles. These other problems include

(i) the flow past a non-spherical fixed particle to gain insight into the shape and angular position dependent drag, lift and torque coefficients ([52, 153, 107, 108, 113, 43] with a spheroid, [52, 132, 100, 67] with a finite-size cylinder and [111, 52, 87] with a polyhedron), (ii) the flow past a random array of non-spherical fixed particles to understand drag, lift and torque coefficient modulations through neighboring particle flow disturbances ([78] with spheroids, [124, 114] with spherocylinders and [13] with polyhedrons), and (iii) the free settling of a single non-spherical particle to investigate path trajectories and wake instabilities ([92] with a spheroid, [16] with a finite-size cylinder and [103, 118] with a polyhedron). The PR-DNS of flows laden with non-spherical particles require more spatial resolution than the counterpart with spheres, and therefore larger computing resources, while the problem of collisions of non-spherical particles is addressed at length in Chap 7. The analysis of the flow might also be slightly more challenging with non-spherical particles than with spheres, but we believe that the PR-DNS of flows laden with non-spherical particles is primarily a high performance computing problem. With the increasing power offered by supercomputers, we expect to see more contributions to the literature in the near future on this topic.

### 6.3 PR-DNS of unbounded flows in the dilute regime

In the present section we consider the collective dynamics of particles suspended in a body of fluid far from any solid boundaries, focusing on the dilute regime. In a first part we will focus on systems where the fluid is initially at rest, and in a second part on configurations where the background flow corresponds to the classical homogeneous isotropic turbulence.

#### 6.3.1 Settling in initially ambient fluid

The behavior of a single particle settling in ambient fluid is a surprisingly rich topic, as a variety of path regimes arise in different parts of the parameter space (density ratio, Galileo number, particle shape), with the single particle settling e.g. straight, vertically, on a straight oblique path, with time-periodic oscillations, in zig-zag or chaotically. This topic has been exhaustively studied in the past, either experimentally or numerically, in the latter case typically with the aid of interface-conforming methods (cf. the review by [31]).

When a collective of particles is considered, the nature of the interaction becomes even more complex and is still an object of active research. The most striking features concern the formation of clusters due to particle interaction and the possible increase or decrease of the settling velocity, which requires to be properly defined. In this case, the settling velocity  $W_{rel}^{(i)}$  of the  $i^{th}$  particle corresponds to the relative velocity between a particle and the fluid velocity averaged in the entire domain, and reads (supposing that gravity acts in the negative  $z$ -direction):

$$W_{rel}^{(i)}(t) = V_{p,z}^{(i)}(t) - \langle u_{f,z} \rangle_{V_f}(t) \quad (6.4)$$

where  $\langle \mathbf{u}_f \rangle_{V_f}$  is the fluid velocity averaged over the volume occupied by the fluid.  $W_{rel}$  is then the value obtained once ensemble averaging (6.4) over all particles, and  $W_s$  henceforth denotes the terminal velocity of an isolated particle.

Figure 6.4 gathers results from the literature on the evolution of the settling velocity at different particle volume fraction and Galileo numbers. The settling of many spheres in an initially ambient fluid has been first numerically investigated with DNS by Kajishima & Takiguchi [64] for single sphere particle Reynolds number  $Re_{ps}$  ranging from 50 to 400 and density ratio  $\rho_p/\rho_f = 8.8$ . They used periodic boundary conditions in the three directions and neglected particle rotation. They observed

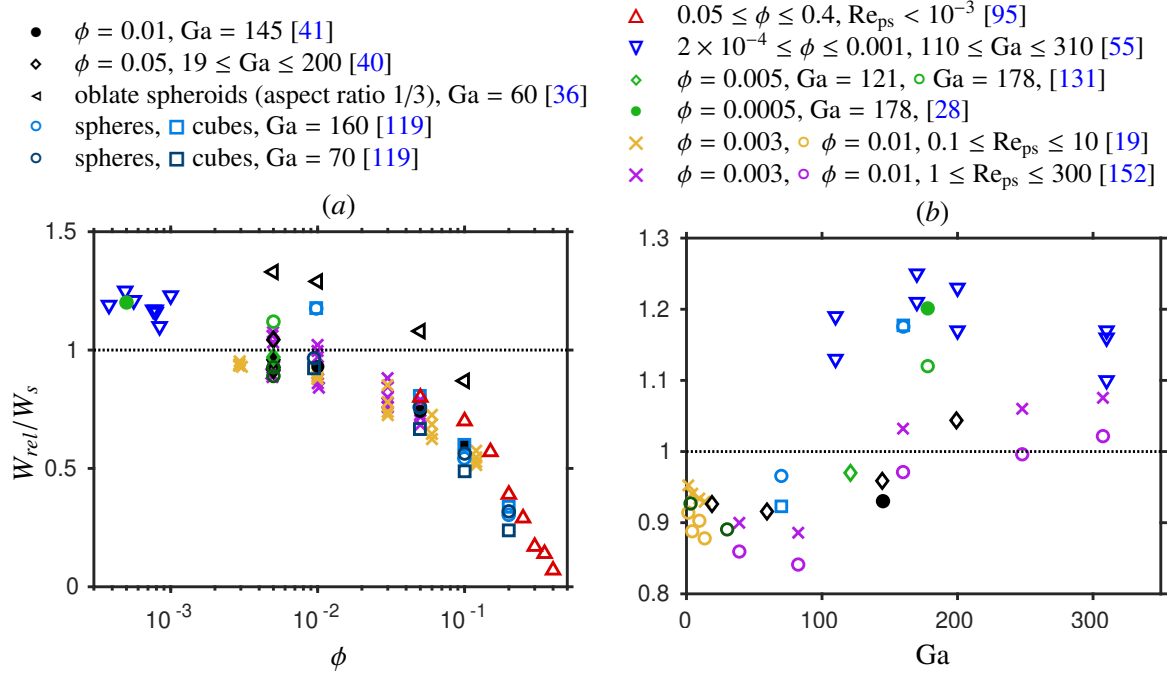


Figure 6.4: Evolution of the mean particle settling velocity  $W_{rel}$  scaled by the corresponding single-sphere value  $W_s$  for different simulations and experiments in ambient fluid represented as a function of the solid volume fraction (a) and Galileo number (b). When not mentioned in the legend, the data refers to spherical particles. Colorstyle is common for (a) and (b), data from references [19] and [152] are represented exclusively with crosses on (a).

the formation of columnar clusters for  $Re_{ps}$  larger than 100 and a global decrease of the drag coefficient, attributed to wake interactions, with the effect to globally increase the settling velocity. Later Kajishima [63] explored similar configurations while accounting for particle rotation and considering larger computational setups at  $Re_{ps} \approx 300$ . This work confirmed the formation of columnar clusters with rotational particles with a slightly smaller increase in settling velocity. Uhlmann & Doychev [131] later focused on the influence of the settling regime. They considered two configurations featuring the same solid volume fraction ( $\phi = 5 \times 10^{-3}$ ) but two different single-sphere settling regimes: a steady axi-symmetric regime with  $Ga = 121$  and a steady oblique regime with  $Ga = 178$ . They showed that particles tend to cluster into columns only for the steady oblique regime, leading to a global increase of the settling velocity. The experimental work of Huisman et al. [55] has confirmed that the cluster formation into columns does not constitute a numerical artifact. They investigated Galileo numbers ranging from 110 to 310 and showed that for  $Ga \geq 170$  particles tend to align vertically, while the cluster formation stays relatively weak at  $Ga = 110$ . The level of clustering was quantified with the aid of Voronoï tessellation analysis, as introduced by Monchaux et al. [90], and described in chapter 2. Such analysis has been previously used in the work of Uhlmann & Doychev [131] for finite-size particles. Note that it was shown in [129] that great care has to be taken in the analysis to account for finite size effects, since the constraint of non-overlapping particles and the number of particles both affect the reference of randomly positioned particles. It is also necessary to consider large computational domains as it might affect the formation of clusters.

The picture is different when the particle volume fraction increases or when the Galileo number decreases as represented on figure 6.4. Climent & Maxey [19] and Zaidi et al. [152] numerically

observed a decrease of the settling velocity for these cases, with a similar trend as experimentally shown by Nicolai et al. [95] at very small settling Reynolds numbers ( $\text{Re}_{\text{ps}} \leq 10^{-3}$ ). This velocity decrease is usually attributed to the fact that settling generates an upward flow to compensate for the particle downward motion and ensure zero mixture velocity. This phenomenon is known as the hindrance effect for which Richardson & Zaki [106] proposed an approximation by a power law of type

$$W_{\text{rel}}/W_s = (1 - \phi)^n, \quad (6.5)$$

based on experimental data. In [40] a set of Galileo numbers ranging from 19 to 200 with density ratios close to unity (ranging from 1.0035 to 1.038) was investigated and a global decrease of  $W_{\text{rel}}$  compared to  $W_s$  was observed for particles settling in the steady axi-symmetric regime, while particles at  $\text{Ga} = 200$  settle with a higher velocity. Later Fornari et al. [41] focused on the case  $\text{Ga} = 145$  with different particle volume fractions and observed a decrease of  $W_{\text{rel}}$  with  $\phi$  which can reach 60% of its single-particle value at  $\phi = 1\%$ .

The recent numerical work of Seyed-Ahmadi & Wachs [119] have shown that this transition from an increase of the settling velocity at very low particle volume fraction to hindrance effect at larger  $\phi$  seems to take place for spheres and cubes at  $\text{Ga} = 160$ , while spheres and cubes falling at  $\text{Ga} = 70$  only show a decrease of  $W_{\text{rel}}$ . Here again the settling regime of a single particle seems to play a significant role since sphere and cube respectively fall in the steady oblique and helical regime at  $\text{Ga} = 160$  while both sphere and cube follow a vertical path at  $\text{Ga} = 70$ .

One of the major advantages of numerical simulation is that it gives us access to the velocity field in the vicinity of each particle, opening with it the discussion on the flow conditions actually experienced by each particle. This leads to a distinction between two definitions of the settling velocity. As mentioned above, the first definition  $W_{\text{rel}}$  considers the volume averaged velocity  $\langle \mathbf{u}_f(t) \rangle_{V_f}$  to be relevant for the fluid phase. But here the flow is not uniform, and the formation of clusters is expected to create large zones of downward fluid motion in clusters and upward motion in low-concentration regions. Kidanemariam et al. [69] introduced another definition in which the velocity relevant for the fluid phase corresponds to the fluid velocity  $\mathbf{u}_f^{S_i}(t)$  averaged on a spherical shell centered at the particle position. Tests on the influence of the shell diameter  $d_p^S$  performed for a uniform unbounded flow past a sphere indicated that a radius of  $1.5d_p$  gives the best compromise [69]. Indeed, if  $d_p^S$  is too small then the mean velocity is dominated by the wake of the corresponding particle while the velocity computed with a large  $d_p^S$  would not be representative of the flow actually seen by the particle. Due to finite-size effects the system is strongly two-way coupled and inhomogeneous at the particle scale so that this shell-averaged velocity is different from the "undisturbed" and the "free stream" velocities as discussed in chapter 7. This velocity is also conceptually different from the filtered velocity used in methods relying on volume-filtered field (see for instance chapter 11) as the average is only computed on a shell to minimize self-disturbance contributions. The corresponding settling velocity is defined as follows for a given particle

$$W_{\text{rel}}^{S(i)}(t) = V_{p,z}^{(i)}(t) - u_{f,z}^{S_i}(t), \quad (6.6)$$

and  $W_{\text{rel}}^S(t)$  refers to the velocity obtained once ensemble averaging (6.6) over the particles. Uhlmann & Doychev [131] observed that the particle-averaged settling velocity  $W_{\text{rel}}^S(t)$  is comparable to the corresponding single particle value  $W_s$  with and without cluster formation. As the fluid velocity within clusters is mostly directed downwards, the enhancement of  $W_{\text{rel}}$  could simply be the effect of preferential sampling of the flow. The experimental work of Huisman et al. [55] confirms this trend



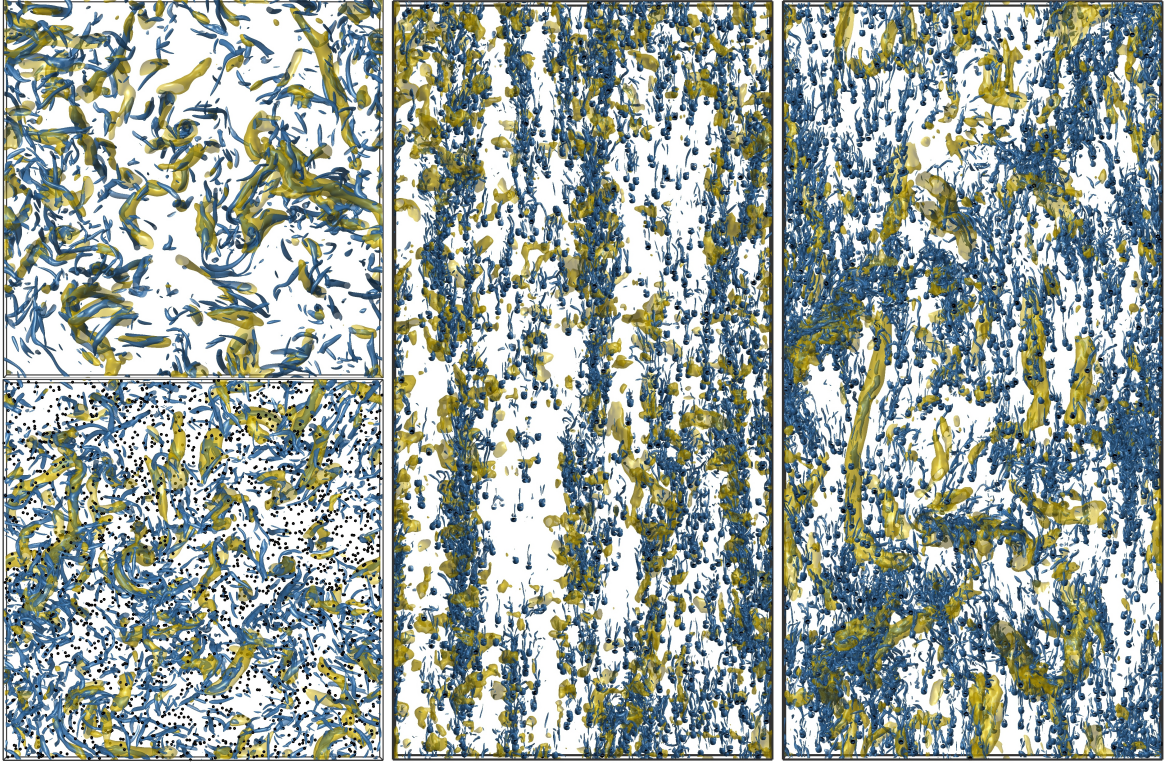


Figure 6.5: Visualization of the flow structure taken from Chouippe & Uhlmann [15]: Isocontour of the  $Q$  criterion for the unfiltered field (blue) and the field box-filtered at a scale  $\Delta_{filt}$  (yellow) for a single-phase case at  $Re_\lambda = 95$  (top left), for  $Ga = 0$  and  $Re_\lambda = 120$  (bottom left,  $\Delta_{filt} = 3.7d_p$ ),  $Ga = 178$  and ambient flow (center,  $\Delta_{filt} = 5.6d_p$ ),  $Ga = 180$  and  $Re_\lambda = 142$  (right,  $\Delta_{filt} = 5.6d_p$ ). The visualizations represent the total domain in the vertical plane and one eighth of the domain in the horizontal plane (into the page).

since particles with small Voronoi volumes are shown to fall with an increased Reynolds number while particles with large volumes tend to settle with a decreased velocity. This decrease of velocity in low density regions can be attributed to the formation of upward flow regions outside of clusters.

Less is known on the properties of the pseudo-turbulence generated by the particles while they settle, and the detailed characteristics of these fluctuations are nowadays still the object of speculations. Numerical work of Kajishima & Takiguchi [64] and Doychev [28] indicates that this turbulence displays similar properties as turbulence generated by the rise of bubbles in a quiescent flow, which has been described by Risso [109]. Riboux et al. [105] have already shown experimentally that a random set of fixed spheres generates turbulence featuring the same structure as a rising bubble cloud. The turbulence as described by Risso [109] results in the superposition of Gaussian wake contributions, leading to a turbulence energy spectrum featuring a  $-3$  power law. This type of energy spectra has been numerically observed [28], which tends to indicate that similar wake influence is at play.

### 6.3.2 Finite-size particles in turbulent background flow

We consider now configurations where the carrying flow is still unbounded but turbulent, focusing on the idealized configuration of homogeneous-isotropic-turbulence as represented on figure 6.5, where



the typical worm-like turbulent structures are made visible by representing iso-surfaces of the Q-criterion. Such flows are usually generated in simulations by the use of a forcing term in the momentum equation of the Navier-Stokes equations, and mainly two types of schemes have been used in the literature: it either depends on flow characteristics such as velocity field or dissipation rate, or it can be independent of the flow field. The second category is usually preferable in the presence of finite-size particles, as the system might become unstable due to two-way coupling effects. Most of these external forcings are formulated in spectral space and consist in randomly injecting energy in the largest eddies of the system [35].

In the absence of gravity ( $Ga = 0$ ), the main questions addressed in the literature mostly concern the possible formation of particle clusters, and scaling of particle acceleration and velocity, focusing on the deviation from the point-particle limit. Uhlmann & Chouippe [130] have numerically investigated configurations featuring two different Reynolds numbers ( $Re_\lambda = 115$  and  $140$ ) with particles larger than the Kolmogorov lengthscale ( $d_p/\eta = 5, 11$ ) and slightly denser than the fluid ( $\rho_p/\rho_f = 1.5$ ), in the dilute regime ( $\phi = 0.005$ ). The corresponding Stokes numbers are larger than unity if based on the Kolmogorov time-scales ( $St_\eta = 2.5, 10.7$ ) and smaller than unity if based on the large-eddy turnover time ( $St_T = 0.06, 0.29$ ). With the aid of Voronoï tessellation analysis a weak formation of clusters was shown [130] and the authors analyzed particle position with respect to the position of 'sticky-points' [49]. Those points verify  $\mathbf{e}_1 \cdot \mathbf{a}_f = 0$  and  $\lambda_1 > 0$ , where  $\mathbf{a}_f$  denotes the fluid acceleration,  $\lambda_1$  is the largest eigenvalue and  $\mathbf{e}_1$  the corresponding eigenvector of the symmetric part of the acceleration gradient tensor (cf. also chapter 2). The analysis shows a small but statistically significant increase of the probability of finding 'sticky-points' in the particles' vicinity, implying that a clustering mechanism similar to the sweep-stick mechanism [49] might be at play. Note that the authors in [130] have not found any significant direct evidence of the centrifugal mechanism [82] at work.

Turning now to the evolution of particle velocity and acceleration, the shapes of their p.d.f. seem to be relatively well established in the literature but not their variance. The normalized p.d.f. of single velocity components appears to be Gaussian as the carrying fluid [130, 53, 145], and the p.d.f. of acceleration has been shown to follow a universal shape related to a lognormal distribution of the magnitude of the particle acceleration [91, 101]. The relative difference between the particle and fluid velocity variance has been first shown to follow a  $d_p^{2/3}$  power law [53] for  $d_p \gtrsim 5\eta$ , which has been later also observed by Uhlmann & Chouippe [130] for  $d_p \gtrsim 3\eta$ . Different trends have been observed for the acceleration variance: experimental work in Von Kármán flow [136, 8, 134] or in a wind tunnel [101] exhibited a  $(d_p/\eta)^{-2/3}$  or  $(d_p/\eta)^{-0.81}$  power-law at large flow Reynolds number, while DNS performed at lower  $Re_\lambda$  exhibits an evolution proportional to  $(d_p/\eta)^{-4/3}$  [53, 17, 130]. A  $(d_p/\eta)^{-2/3}$  power law can be attributed to the fact that particle acceleration is mostly affected by flow scales of the order of  $d_p$ , with a correction accounting for intermittency leading to the  $(d_p/\eta)^{-0.81}$  power-law, while an evolution in  $(d_p/\eta)^{-4/3}$  seems to be the effect of the largest scale that predominantly affect particle motion through sweeping mechanisms.

In the absence of gravity and in the dilute regime, particles have been shown to have little influence on the flow statistics [130] so that the flow can globally be considered as nearly one-way coupled even for particles larger than  $\eta$ . But this is not the case anymore in the presence of gravity, and an important parameter in that case is the relative turbulence intensity  $I = u_{rms}/W_s$ , namely the ratio between the characteristic velocity of the background forced turbulence and the settling velocity of an isolated particle in quiescent flow. This can be explained by considering the global energy balance: for this we introduce the instantaneous kinetic energy  $E_k(t) = \mathbf{u} \cdot \mathbf{u}/2$  (where  $\mathbf{u}$  refers to the composite velocity field defined throughout the joint volume occupied by either the fluid or the particles) and the

time rate of change of its volume average [14]:

$$\frac{d\langle E_k \rangle_{V_\infty}}{dt} = -\varepsilon_{V_\infty} + \psi^{(turb)} + \psi^{(p)} \quad (6.7)$$

where  $\varepsilon_{V_\infty}$  refers to the dissipation rate averaged over the entire volume of the system, and  $\psi^{(turb)}$  and  $\psi^{(p)}$  to the work done by the turbulence forcing used to generate the turbulent background flow and the fluid-particle coupling, respectively. Note that various authors have used alternative forms of the kinetic energy budget in the context of PR-DNS [e.g. 84, 117]. Chouippe & Uhlmann [15] have investigated the settling of particles at  $Ga \approx 180$  in two configurations featuring  $d_p/\eta = 6.8 - 8.5$ ,  $Re_\lambda = 95 - 142.2$ , and turbulence intensities  $I = 0.14 - 0.22$ . They observed that the work done by the turbulence forcing is barely affected by the presence of the particles and that  $\psi^{(p)}$  is dominated by a term  $\psi_{(pot)}^{(p)}$  which arises from the slip velocity between particles and the fluid and is defined as

$$\frac{\psi_{(pot)}^{(p)}}{\varepsilon} = \phi Ga^3 \left( \frac{d_p}{\eta} \right)^{-4} \frac{\langle V_{p,z}^{(i)} \rangle - u_{f,V_\infty}}{u_g}, \quad (6.8)$$

meaning that the dissipation tends to increase under the release of the particles' potential energy while they settle. A first rough estimation of this increase can be obtained based on equation (6.8) under the approximation  $\langle V_{p,z}^{(i)} \rangle - u_{f,V_\infty} \approx W_s$ . It emphasizes the importance of the particle size, particle volume fraction and Galileo number on the modification of the background flow. Such an approximation would then predict that at a given Galileo number the two-phase dissipation would linearly increase with  $\phi$ , which is in accordance with the numerical observation of Fornari et al. [41] at  $Ga = 145$ ,  $d_p/\eta = 12$  and  $Re_\lambda = 90$ . This importance of the contribution associated to slip velocity is also qualitatively in accordance with pseudo-turbulent configurations [85]. The influence of particle clusters on the background turbulence is difficult to isolate as the level of clustering appears to be influenced by the turbulence intensity.

Concerning now the influence of turbulence on particle settling and potential clustering it seems that homogeneous-isotropic turbulence at modest Reynolds numbers acting on particles larger than the Kolmogorov scale globally tends to decrease the level of clustering and the settling velocity compared to equivalent configuration with initially ambient flows [15, 39, 40, 41]. Chouippe & Uhlmann [15] have shown, based on Voronoï tessellation analysis, that forcing turbulence rapidly disturbs the wake-induced columns without completely destroying them, but it does not display a monotonic trend with turbulence intensity. The relative size of the particles with respect to the scales of the forced turbulence seems to play an important role, but the mechanisms at play are still the object of an ongoing discussion, and not all parameters have been systematically swept.

The analysis proposed by Fornari et al. [39] indicates that large particles at low density ratios experience significant non-stationary effects. In a first approximation, one could model the influence of turbulence by adding a Gaussian perturbation with the same standard deviation as the forced turbulence to the velocity seen by the particles. This would lead to the so-called nonlinear drag effect [54, 86, 7], which partially explains the trend of the settling velocity reduction as shown in figure 6.6. Note that this model does neither account for the modification of the flow by the particles, nor for the particle-particle interaction through wake-attractions, nor for crossing trajectories. It is indeed known that the two-way coupled background flow does not feature Gaussian like fluctuations in the vertical direction [15], and as the solid volume fraction increases, turbulence has been shown to have less influence compared to the equivalent quiescent configuration. This last point is most probably to be attributed to the fact that drafting-kissing-tumbling remains relatively frequent at larger solid volume fraction [41]. The relevant time-scales are also difficult to specify through a unique parameter

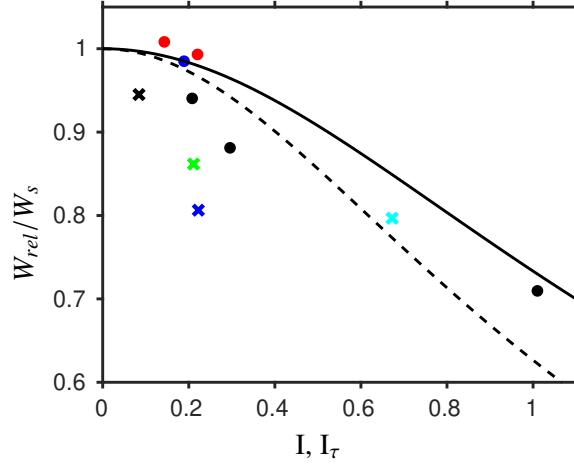


Figure 6.6: The mean settling velocity (normalized by the value for an isolated sphere in ambient fluid) in unbounded systems with forced background turbulence, plotted versus the relative turbulence intensity  $I$ . The filled circles correspond to the parameter triplet  $(\rho_p/\rho_f, Ga, d_p/\eta)$  as follows: • (1.0004 – 1.04, 19 – 200, 12) [40]; • (1.5, 120, 7) [14]; • (1.5, 180, 7 – 9) [15]; all aforementioned cases feature a global solid volume fraction  $\Phi_s = 0.005$  and background flow Reynolds number  $Re_\lambda \sim O(100)$ . The lines indicate the non-linear drag model of [54], evaluated for: —  $Ga = 20$ ; ---  $Ga = 180$ . The data points marked by crosses are taken at the centerline of vertical turbulent channel flow (cf. figure 6.7b below, and the color-coding therein); in the channel flow cases the relative turbulence intensity is defined with the friction velocity  $u_\tau$  as  $I_\tau = u_\tau/W_s$ .

(e.g. Stokes number based on the Kolmogorov timescale  $St_\eta = \tau_p/\tau_\eta$ ), first because particles are most probably affected by eddies larger than  $\eta$  due to their size, and second since settling might decrease the time that particles spend in a given eddy altering the timescale actually perceived by the particles.

## 6.4 PR-DNS of wall-bounded shear flows

Wall-bounded shear flows are relevant to many technical and natural systems, and they are therefore a popular laboratory for particulate flow studies. Due to the presence of at least one inhomogeneous spatial direction, the computational cost is significantly larger than in unbounded set-ups, which explains the relatively recent advent of PR-DNS in this category. One clear advantage of wall-bounded flows is the natural occurrence of turbulence at sufficiently large Reynolds number, which obviates the need for ad hoc forcing. It should be mentioned that the onset of laminar-turbulent transition is greatly influenced by the presence of rigid particles [81]. This process which is the subject of much ongoing research [79, 149, 1], however, reaches beyond the scope of the present text. Furthermore, in the following we will restrict our attention to plane channel flow, since it constitutes the most widely studied geometry. Other flow configurations have also been tackled by means of PR-DNS, e.g. plane Couette flow [142, 2, 102], circular pipe flow [149], rectangular duct flow [38, 151].

### 6.4.1 Vertical plane channel flow

In the present subsection we are considering configurations in which gravity does not directly generate mean gradients in the particle concentration. We are first focusing upon dilute or semi-dilute

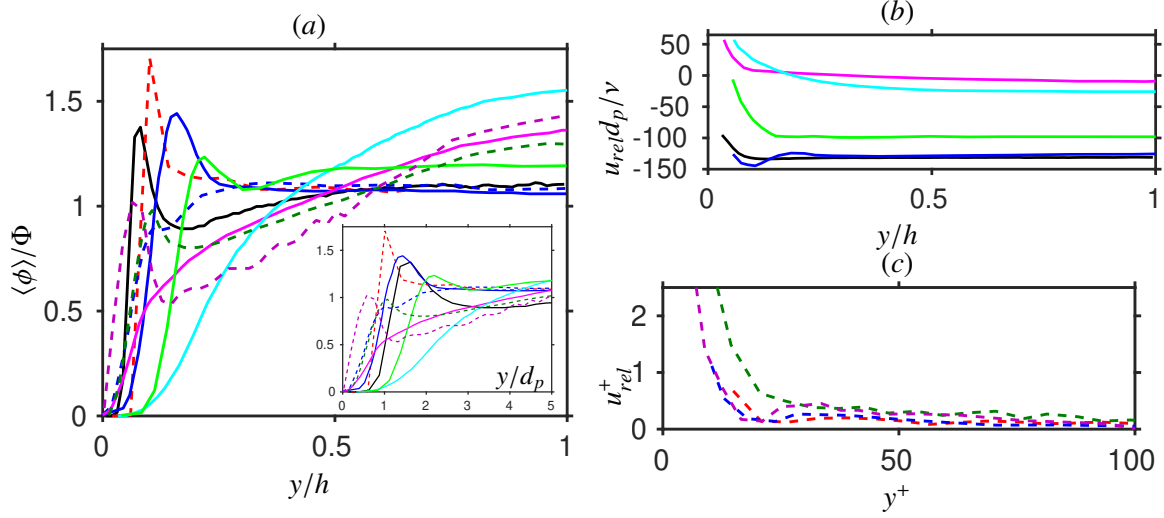


Figure 6.7: (a) Mean particle volume fraction  $\langle\phi\rangle$  (normalized with the global value  $\Phi$ ) in various plane channel flow PR-DNS without gravity effects in the wall-normal direction, plotted as function of wall-distance  $y$ , normalized by channel half-width  $h$ . Solid lines correspond to cases where gravity acts on particles in the primary fluid flow direction, while dashed lines are for cases without gravitational effects. The values for the parameter quadruplet  $(\rho_p/\rho_f, Ga, d_p^+, \Phi_s)$  are as follows: --- (1, 0, 21, 0.05) [34]; --- (2.84, 0, 15, 0.002) [147]; --- (10.4, 0, 18, 0.0084) [148]; --- (10, 0, 22, 0.02) [37]; --- (2, 23, 19, 0.024) [156]; --- (2, 40, 18, 0.024) [156]; --- (2, 99.5, 21, 0.024) [150]; --- (2.2, 115.4, 11.3, 0.0042) [48]; --- (1.15, 126, 28, 0.05) [34]. The bulk Reynolds number measures 2700–2800 over the entire data-set. The inset shows the same data with the wall-distance scaled by the particle diameter. (b) Profiles of apparent velocity lag in the streamwise direction,  $u_{rel} = \langle u_p \rangle - \langle u_f \rangle$ , scaled with the viscous particle velocity, shown for cases with streamwise gravitational effects. (c) Same as (b), but for cases without gravitational settling, scaled in wall units.

suspensions with global particle volume fraction up to  $O(10^{-2})$ , and then we will turn our attention to denser systems. The questions which are most relevant in wall-bounded flows are similar to those in unbounded flow (where do particles go, and what do they do to the flow?) with the added complexity of spatial inhomogeneity and anisotropy of the turbulent background flow. As a starting point let us discuss the mean relative velocity between the two phases, which in the statistically stationary regime now becomes a function of the wall-normal coordinate (henceforth denoted as  $y$ , ranging from 0 to  $2h$ , with  $h$  the channel half-width). Figure 6.7(b, c) shows the apparent relative velocity in the streamwise direction,  $u_{rel} = \langle u_p \rangle - \langle u_f \rangle$ , for a number of data-sets from PR-DNS of upward channel flow [48, 147, 156, 34, 150] conducted with neutrally-buoyant or dense particles at density ratios  $\rho_p/\rho_f = O(1)$ , particle sizes  $d_p^+ = O(10)$  (where the + superscript indicates wall units) and bulk flow Reynolds numbers 2700 to 2800 (based upon the bulk velocity  $u_b$  and channel half width). It can be seen in the figure that the relative velocity is essentially constant over most of the bulk flow region, and that the magnitude of the bulk value generally increases with increasing Galileo number from zero to  $O(100)$ . In order to gauge the effect of turbulence on mean settling, we have included in figure 6.6 the mean settling velocity on the channel centerline of those simulations with finite Galileo number, normalized with the settling speed of an isolated particle in ambient fluid (obtained from equilibrium between drag and submerged weight, resorting to the standard drag law [18]), plotted versus the rel-

ative turbulence intensity now defined as  $I_\tau = u_\tau/u_g$  (where  $u_\tau$  is the mean friction velocity). As in the case of unbounded flow with homogeneous-isotropic forcing, a significant decrease of the settling speed with increasing  $I_\tau$  is observed, which again might be related to the non-linear drag mechanism already discussed in subsection 6.6. Please recall that the global particle volume fraction varies among the present channel flow data points (cf. the caption of figure 6.7), which is expected to contribute to the reduced settling velocity through the Richardson-Zaki hindrance effect.

Interestingly, all curves in figure 6.7(b) exhibit an upward trend when approaching the channel wall, indicating a further reduction of the particle settling velocity in the near-wall region. The same is also true for neutrally-buoyant particles and for dense particles in the absence of gravity (for which both  $Ga = 0$ ), as can be seen in figure 6.7(c). In upward channel flow with heavy particles Uhlmann [128] has attributed this effect to an increase in the quasi-steady drag force when a particle is located at a wall distance of the order of its diameter (cf. drag correlations for a sphere translating near a wall, [154], and for a sphere translating in a linear, wall-bounded shear flow [77]). Other authors have shown that particles near the wall preferentially sample the high-speed regions in upward channel flow with heavy particles [156], as well as in channel flow with dense particles in the absence of gravity [147]. In both cases this sampling bias is consistent with the observed trend, which is reduced when instead computing the mean relative velocity with the fluid velocity measured in the vicinity of the particle.

The next quantity of interest is the mean particle concentration which is shown in figure 6.7(a) for the same parameter points as previously discussed. It can be seen that the shape of the profiles varies strongly, ranging from parabola-like (for dense particles at small but finite Galileo numbers) to nearly flat in the bulk (at large Galileo number, but also for some zero-Galileo cases) with marked local (or global) peaks in the near-wall region. The inset of figure 6.7(a) shows that the near-wall peak occurs at wall-distances between  $0.5d_p$  (particle in contact with the wall) to approximately  $2d_p$ .

A number of mechanisms have been proposed in the literature to account for the mean particle distribution: (i) mean wall-normal (lift) force [128]; (ii) turbophoresis [128]; (iii) collisions [37]. The mean lift effect, which can be decomposed into contributions due to shear, translation and rotation, can be gauged with the aid of the quasi-steady force correlations given by [77]. Esteghamatian & Zaki [34] conclude that the rotational contribution is important in establishing a near-wall peak as it drives particles on the wall-facing edge of a cluster towards the wall, thereby countering the action of shear-induced lift which tends to drive particles in the opposite direction. Uhlmann [128] argued that turbophoresis – the transport of particles down gradients of turbulence intensity [9, 104] – is the main actor which drives particles towards the wall against shear-induced wall repulsion. Fornari et al. [37] argued that in the absence of gravity and for dense particles, collisions are the most effective mechanisms in driving particles towards the channel center. A more complete quantification of the particle distribution has been performed by means of various criteria, such as box-counting [128], nearest-neighbor statistics [65], radial distribution functions [37], and Voronoï tessellation [48, 34]. Thereby, extensive information on the macro and micro-structure of the disperse phase has been obtained, such as evidence of drafting at sufficiently large Galileo number [48, 34]. However, many fundamental questions still remain. It is for example not clear why the (small, heavy) particles in [48] exhibit a slightly more ordered structure than a fully random draw, while those in [34] (which are larger) show a clear degree of clustering. From this short overview it can be concluded that a full understanding of the dynamics leading to the spatial distribution of the disperse phase over the entire parameter space in wall-bounded flows has not yet been achieved.

Now let us briefly discuss particulate channel flow with neutrally-buoyant particles in the dense regime with a global particle volume fraction  $O(10^{-1})$ . Here the contribution from the particle stress becomes comparable to the fluid Reynolds stress in the momentum balance, and the turbulence struc-

ture is significantly modified [99]. Several authors [75, 99, 20, 21] have observed that particles in this case tend to form a relatively dense layer adjacent to the wall, where they also exhibit a significant value of the apparent slip velocity (cf. the discussion on the scaling of the velocity slip in [21]). Separately modelling the stresses in the particle layer and the bulk flow region (where an effective viscosity can be used) then leads to scaling laws for the mean velocity and the wall friction as functions of particle volume fraction and particle size [20]. Lashgari et al. [76] have shown that this reasoning still mostly holds when the disperse phase consists of a binary mixture of small and large particles ( $d_p^+ = 18$  and 24), while the main effect of bi-dispersity lies in the details of the near-wall particle layer.

The literature on wall-bounded turbulence in flows laden with non-spherical particles is rather scarce. Only spheroids of various aspect ratio, spanning both oblate and prolate spheroids, have been considered either in plane channel flows [5, 33, 157, 32, 94, 156] or in pipe flows [50]. To the best of the authors' knowledge, there is no account in the literature of any study involving finite-size cylinders or polyhedrons. The existing body of knowledge on spheroids spans neutrally buoyant [5, 33, 157, 50, 94], non-neutrally buoyant without gravitational effect [32], and non-neutrally buoyant with gravitational effect [156]. The overall picture of the effect of shape via the spheroid aspect ratio when compared to spheres includes the measurable reduction of flow drag and turbulent fluctuations, the stronger migration of spheroids to the center of the channel, the depletion of spheroids in the region close to the wall, the lower angular velocity of spheroids, and the tendency of spheroids to orient parallel to the wall. It is also observed that the more the spheroid aspect ratio deviates from unity [156] or the larger the particle to fluid density ratio is [32] the more pronounced the aforementioned flow features are.

#### **6.4.2 Horizontal plane channel flow**

Here we are interested in the configuration where gravity is directed in the wall-normal direction, such that heavy particles will tend to settle towards the bottom wall. As a direct consequence the mean particle distribution is inhomogeneous, and the details will again depend on their complex interplay with the turbulent shear flow and its coherent structures. This system is particularly relevant to open water bodies (such as rivers and streams), whence the channel is bounded at the top by a free surface.

##### **Focusing of heavy particles in low-speed streaks**

Various experimental and numerical studies have shown that buffer layer coherent structures play an important role in the dynamics of particle motion. Heavy particles, depending on their size, their density and flow Reynolds number, get entrained to the outer flow by the action of the coherent structures. While resettling, the particles are observed to migrate and accumulate into the low-speed fluid regions forming streamwise-aligned streaky particle clusters [62, 96, 120, 69]. In one of the earliest PR-DNS of the configuration, Kidanemariam et al. [69] have shown via conditional averaging that particle lateral motion is strongly correlated with the rotation-sense of a nearby quasi-streamwise vortices. The statistical analysis explains the fact that migration of heavy particles to low-speed streaks is due to the action of the counter-rotating streamwise vortices. It is argued that this phenomenon is the main reason for the observed lower average streamwise particle velocity than the mean fluid velocity in this configuration. As a proof of concept, [98] have recently revisited the above-discussed particle migration into low-speed streaks but by considering equilibrium solutions which feature exact coherent structures (streaks and vortices) to serve as a surrogate of the near-wall turbulent structures. They have shown that particles indeed laterally migrate to the low-speed streaks, demonstrating robustness



of the mechanism.

### Sediment transport

Sediment transport is a dense particulate flow problem which involves the erosion and deposition of sediment grains as a net result of driving hydrodynamic forces and resisting gravity and inter-particle collision forces. Depending on the relative dominance of these forces, sediment grains in a given stream may be stationary or are set in motion by the flow. The onset of sediment motion and subsequent transport is generally believed to be controlled by the Shields number [121]:

$$\Theta = \frac{u_\tau^2}{(\rho_p/\rho_f - 1)|\mathbf{g}|d_p} = \left(\frac{u_\tau}{u_g}\right)^2 = \left(\frac{d_p^+}{Ga}\right)^2, \quad (6.9)$$

where  $|\mathbf{g}|$  and  $d_p$  are the magnitude of acceleration due to gravity and the particle diameter respectively.  $\rho_p/\rho_f$  is the particle to fluid density ratio while  $u_g = \sqrt{(\rho_p/\rho_f - 1)gd_p}$  is the gravitational velocity scale.  $\Theta$  is a measure of the ratio of the total shear force acting on a single grain of the sediment bed to the apparent weight of the particle. For a given flow condition, there is a critical Shields number value  $\Theta_c$  below which the shear force induced by the flow is unable to dislodge and entrain particles from the bed and no sediment erosion is observed.  $\Theta_c$  is known to depend on a number of flow and sediment bed parameters including the Reynolds number of the flow, the constituent sediment grain packing, grain shape, polydispersity, inter-particle contact, etc. At supercritical values of the Shields number ( $\Theta > \Theta_c$ ), larger grains are typically transported close to the bed as ‘bedload’. In bedload transport mode, particles experience regular contact with the bed and move by rolling, sliding or in a series of hopping motions of short duration called saltation. On the other hand, in the case of fine grains or flow with relatively large flow velocities ( $\Theta \gg \Theta_c$ ), particles are generally transported as ‘suspended load’ and remain in suspension for longer times by processes of advection and turbulent diffusion [47]. In the bedload regime, the issuing sediment flux is often expressed as a function of the Shields number (or the excess Shields number  $\Theta - \Theta_c$ ) and various (semi-)empirical predictive models have been proposed [see e.g. 88] and are widely used in engineering practice.

Understanding the physics of sediment transport at the grain scale is imperative to critically assess and improve the various existing predictive models. This is where PR-DNS comes in, which has been increasingly exploited in recent years to simulate subaqueous sediment transport phenomena, both in the laminar and turbulent regimes. Due to the ability of the method to resolve the fluid-particle interaction at the grain scale, PR-DNS has proven to be instrumental in complementing existing experimental and theoretical works by allowing access to relevant quantities. In the following, we briefly review PR-DNS based studies of sediment transport induced by a shearing flow, focusing exclusively on the subaqueous regime, i.e.  $\rho_p/\rho_f = O(1)$ .

Let us remark that performing PR-DNS of sediment transport, even in today’s computing power, is immensely expensive (see example the challenges discussed in section 6.4.2). The ability to faithfully resolve the underlying fundamental mechanisms without modelling comes thus at the cost of simplifying the flow configuration, both in terms of the parameter space and system size. Another aspect of importance is the inter-particle interaction which contributes significantly to the dynamics of the system. In order to realistically account for the collision process between the submerged grains, a discrete element model (DEM) based on either the soft-sphere or hard-sphere approach is usually incorporated to the PR-DNS solution strategy (see details in chapter 7). Some of the earliest contributions have considered the erosion of a sediment bed made up of mono-dispersed spherical particles, induced by shearing laminar flow [25, 72]. These studies were motivated, in part, by the availability of

detailed experimental data to assess the level of fidelity achieved by the numerical approach. Derksen [25] performed PR-DNS of sediment erosion in a Couette flow configuration while Kidanemariam & Uhlmann [72] simulated sediment transport in a laminar Poiseuille covering a wide range of Shields number values. These studies have successfully reproduced experimental observations regarding the threshold for sediment erosion  $\Theta_c$  [97] and the scaling of the sediment particle flux for  $\Theta > \Theta_c$  [6]. Figure 6.8a shows the particle flow rate as a function of the Shields number obtained from the PR-DNS by Kidanemariam & Uhlmann [72], recovering the well-known cubic variation of the particle flow rate with the Shields number for  $\Theta > \Theta_c$ . Furthermore, the direct access to the hydrodynamic and collision forces acting upon individual particles in PR-DNS has enabled the investigation of the rheological proprieties of the mobile sediment bed and the contribution of fluid and particle stresses to the momentum transfer between the two phases [68, 137].

In the turbulent regime, most of available PR-DNS of sediment transport phenomena are at moderate Reynolds number values (friction velocity based Reynolds number  $Re_\tau = O(100)$ ) and have mainly considered a single or a few particles to investigate the role of the near-wall turbulent structures on the entrainment mechanism and subsequent trajectories [93, 10, 138, 58, 146]. There are also studies which consider a few layer of mobile particles to study the collective sediment transport and its modulation of the turbulent flow [59, 60, 139, 26, 140, 141]. Derksen [26] simulated granular bed erosion in a mildly turbulent channel flow and looked at effect of Shields number on the mobility of particles and addressed the role of turbulent fluctuations on particle erosion. Vowinckel et al. [139] considered the transport of sediment particles over a rough bottom and investigated the particle transport patterns and their influence on the bulk statistics of the flow. Extending their work, Vowinckel et al. [140, 141] analysed the momentum balance in a similar setup. Based on the double-average methodology, the latter authors assessed the turbulent and form-induced momentum fluxes as well as boundary stresses contributions to the total budget and the role of mobile particles in the distribution of these stresses. Let us mention that the PR-DNS of turbulent flow over a thick layer of mobile sediment by Kidanemariam & Uhlmann [71] and subsequent publications are discussed in the context of pattern formation in the next section 6.4.2.

Most available PR-DNS of sediment transport have considered spherical particles. However, it is known that particle shape and orientation are important parameters of the flow configuration. There are recent PR-DNS-based studies that address this issue and consider non-spherical sediment grains [45, 44, 155, 56, 57]. For instance, Jain et al. [57] have considered ellipsoidal particles to investigate the effect of particle shape on their trajectories, pickup, erosion and deposition rates and the resulting collective effect (cf. figure 6.8b) These studies highlight the promising prospect of PR-DNS to tackle complex sediment transport phenomena in the near future.

## **Sediment pattern formation**

Probably the most notable achievement of PR-DNS in the context of sediment transport has been the ability to simulate the phenomenon of sediment pattern formation [71, 73, 83, 115, 57, 70, 116]. The process of local erosion of particles from an erodible sediment bed and their deposition at certain preferential locations often leads to the formation of sediment patterns or bedforms. Sediment patterns are observed at a wide range of spatial and temporal scales in a variety of environments such as deserts, river and marine flows as well as various technical applications involving shear flow over an erodible sediment bed. It is highly desirable to accurately predict the formation processes of bedforms as they have important implications for instance in waterway management, planning and maintenance of various hydraulic structures and geophysics. Capturing sediment pattern formation and evolution via PR-DNS is immensely challenging due to the much larger spatial and temporal scales of the

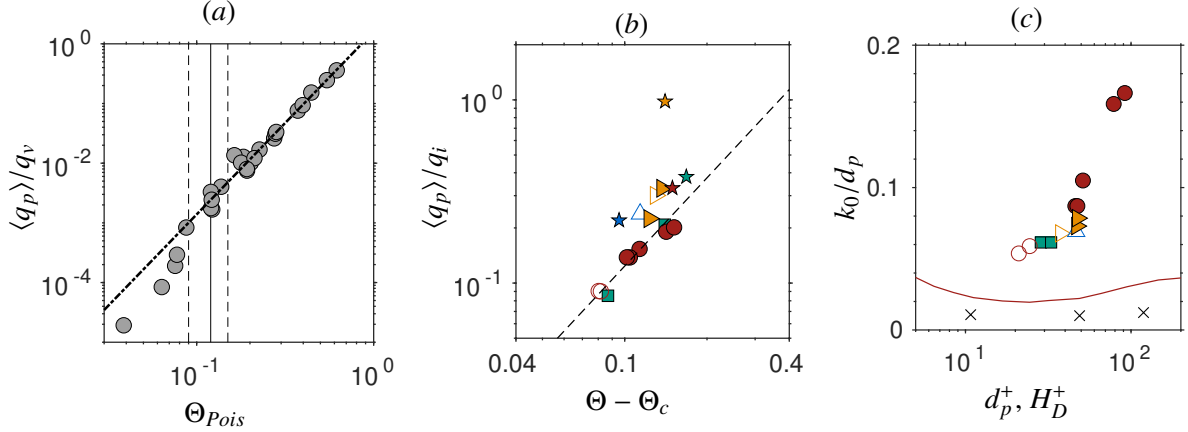


Figure 6.8: (a) PR-DNS of a sediment bed sheared by laminar channel flow: Mean volumetric particle flow rate  $\langle q_p \rangle$ , non-dimensionalized by the viscous scaling  $q_v = Ga^2 \nu$ , as a function of the Shields number defined based on the laminar plane Poiseuille flow over a smooth wall, viz  $\Theta_{Pois} = 6Re_b/Ga^2(d_p/H_f)^2$ .  $\bullet$ ,  $Re_b = 110\text{--}500$ ,  $Ga = 6\text{--}15$ ,  $H_f/d_p = 7.5\text{--}20$ ,  $\rho_p/\rho_f = 2.5$  [72]. The vertical solid/dashed lines indicate the critical Shields number for particle erosion  $\Theta_{Pois}^c = 0.12 \pm 0.03$  [97]. The chain-dotted line corresponds to a power law fit proportional to  $\Theta_{Pois}^3$ . (b) PR-DNS of sediment bed erosion in turbulent channel flow. Volumetric particle flow rate  $\langle q_p \rangle$  (normalized by the inertial scale  $q_i = u_g d_p$ ) as a function of the excess Shields number  $\Theta - \Theta_c$ . The critical Shields number  $\Theta_c$  is obtained using the empirical law proposed by Soulsby & Whitehouse [122].  $\bullet$  ripple-featuring,  $\circ$  ridge-featuring,  $Ga = 28$ ,  $H_f/d_p = 25$ ,  $\rho_p/\rho_f = 2.5$ ,  $d_p^+ = 9\text{--}12$ ;  $\blacksquare$  ripple-featuring,  $Ga = 17\text{--}20$ ,  $H_f/d_p = 50$ ,  $\rho_p/\rho_f = 2.5$ ,  $d_p^+ = 7$ ;  $\triangle$  featureless,  $Ga = 105$ ,  $H_f/d_p = 8$ ,  $\rho_p/\rho_f = 2.5$ ,  $d_p^+ = 39$ ;  $\blacktriangleright$  ripple-featuring,  $\blacktriangleright$  featureless,  $Ga = 44\text{--}57$ ,  $H_f/d_p = 12\text{--}16$ ,  $\rho_p/\rho_f = 2.5$ ,  $d_p^+ = 17\text{--}23$  [73, 115]. The star symbols correspond to the PR-DNS of ellipsoidal particles ( $\star$ , Zingg ellipsoid;  $\star$ , prolate;  $\star$ , oblate;  $\star$ , sphere)  $Ga = 45$ ,  $H_f/d_p = 16\text{--}18$ ,  $\rho_p/\rho_f = 2.55$ ,  $d_p^+ = 16\text{--}20$  [57]. The dashed line is the Wong & Parker [144] version of the Meyer-Peter & Müller [88] formula for turbulent flows:  $q_p/q_i = 4.93 (\Theta - \Theta_c)^{1.6}$ . (c) The hydrodynamic roughness length  $k_0$ , obtained by fitting the relation  $\langle u_f \rangle^+ = 1/\kappa \log((y - y_0)/k_0)$  to the fluid mean velocity profiles of the corresponding PR-DNS cases in 6.8b, as a function of the inner-scaled sediment bed roughness height  $H_D^+$  ( $H_D$  is the crest-to-trough height of the extracted two-dimensional sediment bed interface). The cross symbols ( $\times$ ) represent values of  $k_0$  as a function of  $d_p^+$  of a single-phase flow over fixed spheres arranged on a square lattice [11]. The solid line is the model prediction  $k_0$  as a function of  $d_p^+$  by Duran Vinent et al. [29].

patterns (compared to the particle scale) which need to be resolved. In order to realistically capture the patterns, large computational domains involving up to  $O(10^{10})$  grid nodes are required. Moreover, a thick erodible sediment bed composed of at least  $O(10^5)\text{--}O(10^7)$  particles must be considered in order to accommodate patterns. At the same time, the ratio between the particle size and the grid cell width should be adequately large (typically  $d_p/\Delta x = O(10)$ ) in order to resolve the near-field flow evolving around individual particles. The evolution time scales of the patterns is another constraint which requires simulation integration times of at least  $O(10^3)$  bulk time units. The above factors pose severe computational challenge and current PR-DNS simulations are so far mainly restricted to the initial patterns formation and evolution stages only.

Customarily, the flow over an erodible bed has been theoretically treated as a hydro-morphodynamic instability problem and is usually tackled by linear stability analysis. The hydrodynamics is coupled

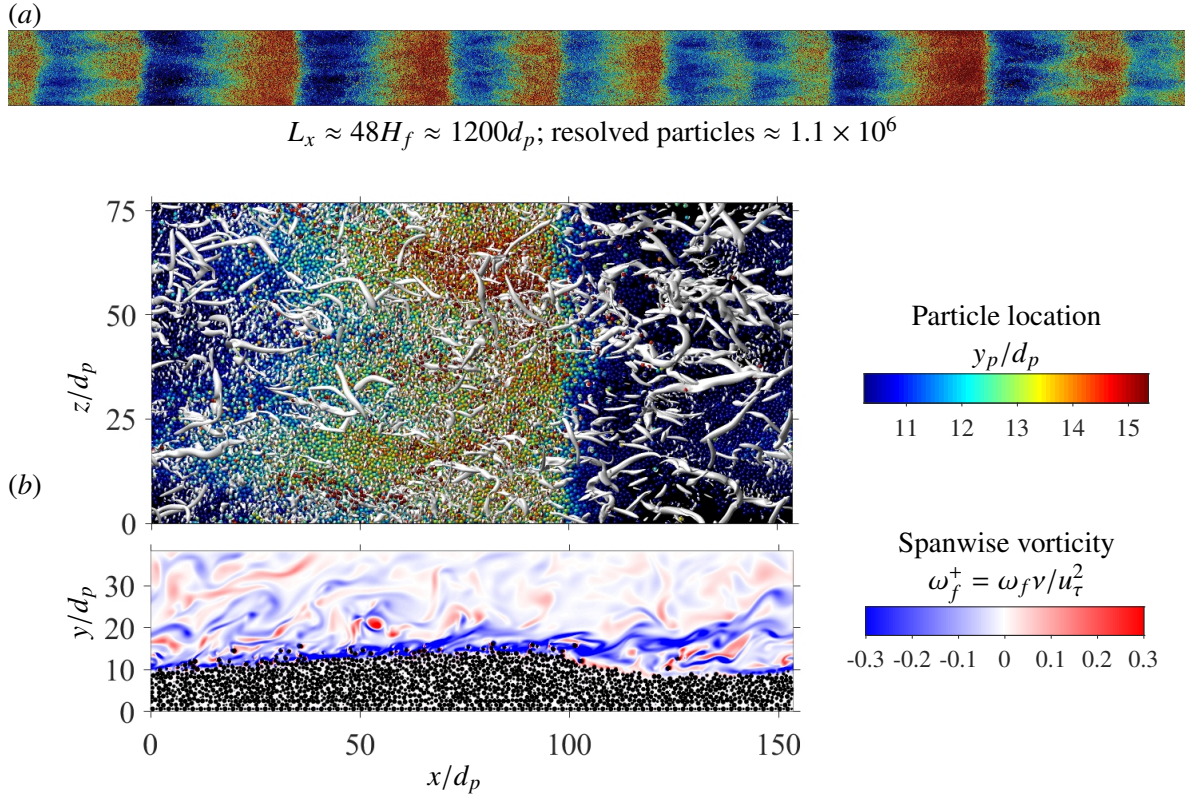


Figure 6.9: Instantaneous visualisations of the flow field and particle positions in a turbulent channel flow over an evolving sediment bed.  $Re_b = 3010$ ;  $Ga = 28.4$ ;  $H_f/d_p = 25$ ;  $\rho_p/\rho_f = 2.5$ ;  $Re_\tau = 240$ – $310$ ;  $d_p^+ = 9$ – $12$  [73, 70]: (a) Top view of the sediment bed which is represented by approximately 1.1 million spherical particles, accommodating a series of self-forming transverse ripples that have formed after approximately 400 bulk time units after initial particle release. Sediment grains are coloured according to their wall-normal location  $y_p$ . Flow direction is from left to right. (b) Snapshot of the near-wall turbulent vortical structures over a single sediment ripple unit (which was forced to steadily evolve in a box size of  $L_x \approx 150d_p$ ) along with the corresponding spanwise vorticity shown on a select wall-perpendicular plane. The strong modulation of the turbulent flow by the evolving sediment bed is highlighted by the increased turbulence intensity downstream of the crest of the ripple.

to the morphodynamic evolution of the bed by an algebraic expression for the particle flux as a function of the Shields number and prediction is made regarding the stability of the sediment bed, the controlling parameters of the instability as well as the initial pattern wavelength [12, 4]. However, the prediction is mostly unsatisfactory which can be linked to, among others, the deficiency of the adopted algebraic expressions for the particle flux. Furthermore, the subsequent evolution of the bedforms and the interaction with the background turbulent flow is not captured by linear analysis. PR-DNS is being increasingly utilised to tackle some of these outstanding questions. Kidanemariam & Uhlmann [71, 73] and later Scherer et al. [115] carried out PR-DNS of the formation of sediment patterns in a channel flow configuration considering a very large number of mobile sediment grains focusing on the initial wavelength selection mechanism, identifying the lower threshold of unstable wavelength and its scaling as well as aspects of the steady non-linear evolution, ripple migration velocity and ripple morphological characteristics. Kidanemariam et al. [70] have further analysed the modulation of the



turbulent flow by the evolving sediment bed (cf. figure 6.9 which clearly show the complex feedback between the flow and the evolving sediment bed). In particular, an evaluation of the local momentum budget was carried out to scrutinise the spatial variation of the boundary shear stress variation. The accurate determination of this quantity, which is one of the main ingredients in models of sediment bed morphology, has been an outstanding issue. The analysis has shown that the shear stress is maximum at a location upstream of the crests exhibiting a positive phase shift with respect to the ripple geometry while the spatially-resolved particle flux lags the shear stress. The phase lag of the particle flux with respect to the shear stress is a consequence of sediment inertia, i.e. a relaxation of the sediment flux to changes in the shear stress [12].

Central in many sediment transport models are the algebraic expressions which relate the mean particle flux  $\langle q_p \rangle$  with the Shields number. PR-DNS data has been recently used to assess the validity of such models [71, 73]. Figure 6.8b shows PR-DNS results of the variation of  $\langle q_p \rangle$  as a function of the excess Shields number  $\Theta - \Theta_c$  from different cases of a sheared sediment bed with and without bedforms. It can be seen that the mean particle flow rate is well predicted by power-law type formulas such as that by Wong & Parker [144]. Nevertheless, as has been recently reported by [70], such power laws are unable to predict the local relationship between the particle flux and the shear stress as a consequence of sediment flux relaxation.

Turning to the the feedback of the evolving rough sediment bed on the turbulent flow, one way of quantifying it is to scrutinise the influence on the vertical variation of the mean fluid velocity profile  $\langle u_f \rangle$ . Commonly,  $\langle u_f \rangle$  in the logarithmic layer is expressed through the definition of a hydrodynamic roughness height  $k_0$  as  $\langle u_f \rangle^+ = 1/\kappa \log((y - y_0)/k_0)$  where  $\kappa = 0.41$  is the von Kármán coefficient and  $y_0$  is some reference origin [61]. The majority of the available sediment morphodynamic models strongly depend on the roughness parameter  $k_0$  [12], and make use of classical correlations of  $k_0$  versus particle Reynolds number  $d_p^+$  which are obtained, for example, from flows over stationary roughness elements (see e.g [29]). However, as is demonstrated in figure 6.8c, the motion of the sediment bed and the evolving ripples substantially increase the value of  $k_0$  for essentially the same value of  $d_p^+$ . For comparison,  $k_0$  values obtained from PR-DNS of the flow over stationary roughness [11] are also shown in the figure.

## 6.5 Conclusions and Outlook

The present review shows that the PR-DNS approach is on an equal footing with laboratory experimental measurements, and that data-sets from both types of sources can be used in a complementary fashion in order to improve our understanding of particulate flow problems. For the future it can be expected that the application of PR-DNS will further expand to encompass additional physical phenomena, as well as growing system sizes which will then allow to cover the large parameter space more extensively. One obvious obstacle here is the sheer size of the data which has made the process of extracting physical insight from raw simulation output an arduous task. Furthermore, the research community has only relatively recently begun to utilize PR-DNS results for the purpose of model development [126]. Applying modern methods from data science to the growing body of data resulting from PR-DNS will provide a promising way forward (cf. related discussion in chapter 14). Another technique – which has not been used extensively in this context in the past – is the method of “numerical experiments” [89]. The possibility to simulate the “wrong physics” in PR-DNS in order to elucidate a specific mechanism is a powerful technique indeed. Several authors have already employed this method in the past (e.g. suppressing particle rotation in order to find out its impact on the particle dynamics [63]; varying the computational domain size in order to find threshold length scales

of the physical system, cf. § 6.4.2), and it is deemed potentially fruitful to design further numerical experiments of this kind. Finally, let us state yet another approach for reducing the complexity of the system investigated with the aid of PR-DNS. Instead of tackling fully developed turbulent flow, one can study particles interacting with one of a growing set of known invariant solutions to the Navier-Stokes equations [66, 98], some of which have been shown to be statistically relevant to turbulence. While the combination of PR-DNS and invariant solutions has not yet demonstrated its full potential, it appears as a worthwhile avenue to explore.



# Bibliography

- [1] Agrawal, N., Choueiri, G., & Hof, B. (2019). Transition to turbulence in particle laden flows. *Phys. Rev. Lett.*, [122](#), 114502.
- [2] Alghalibi, D., Lashgari, I., Brandt, L., & Hormozi, S. (2018). Interface-resolved simulations of particle suspensions in Newtonian, shear thinning and shear thickening carrier fluids. *J. Fluid Mech.*, [852](#), 329–357.
- [3] Alvelius, K. (1999). Random forcing of three-dimensional homogeneous turbulence. *Phys. Fluids*, [11](#), 1880–1889.
- [4] Andreotti, B., & Claudin, P. (2013). Aeolian and subaqueous bedforms in shear flows. *Philos. Trans. A. Math. Phys. Eng. Sci.*, [371\(2004\)](#), 20120364.
- [5] Ardekani, M. N., Costa, P., Breugem, W.-P., Picano, F., & Brandt, L. (2017). Drag reduction in turbulent channel flow laden with finite-size oblate spheroids. *J. Fluid Mech.*, [816](#), 43–70.
- [6] Aussillous, P., Chauchat, J., Pailha, M., Médale, M., Guazzelli, É., & Guazzelli, É. (2013). Investigation of the mobile granular layer in bedload transport by laminar shearing flows. *J. Fluid Mech.*, [736](#), 594–615.
- [7] Bagchi, P., & Balachandar, S. (2003). Effect of turbulence on the drag and lift of a particle. *Phys. Fluids*, [15\(11\)](#), 3496–3513.
- [8] Brown, R., Warhaft, Z., & Voth, G. (2009). Acceleration statistics of neutrally buoyant spherical particles in intense turbulence. *Physical Review Letters*, [103\(19\)](#).
- [9] Caporaloni, M., Tampieri, F., Trombetti, F., & Vittori, O. (1975). Transfer of particles in nonisotropic air turbulence. *J. Atmosph. Sc.*, [32](#), 565–568.
- [10] Chan-Braun, C. (2012). *Turbulent open channel flow, sediment erosion and sediment transport*. Ph.D. thesis, Karlsruhe Institute of Technology.
- [11] Chan-Braun, C., García-Villalba, M., & Uhlmann, M. (2011). Force and torque acting on particles in a transitionally rough open-channel flow. *J. Fluid Mech.*, [684](#), 441–474.
- [12] Charru, F., Andreotti, B., & Claudin, P. (2013). Sand Ripples and Dunes. *Annu. Rev. Fluid Mech.*, [45\(1\)](#), 469–493.
- [13] Chen, Y., & Müller, C. R. (2018). Development of a drag force correlation for assemblies of cubic particles: The effect of solid volume fraction and Reynolds number. *Chemical Engineering Science*, [192](#), 1157–1166.
- [14] Chouippe, A., & Uhlmann, M. (2015). Forcing homogeneous turbulence in DNS of particulate flow with interface resolution and gravity. *Phys. Fluids*, [27\(12\)](#), 123301.

- [15] Chouippe, A., & Uhlmann, M. (2018). On the influence of forced homogeneous-isotropic turbulence on the settling and clustering of finite-size particles. *Acta Mechanica*, [230\(2\)](#), 387–412.
- [16] Chrust, M., Bouchet, G., & Dušek, J. (2013). Numerical simulation of the dynamics of freely falling discs. *Physics of Fluids*, [25](#), 044102.
- [17] Cisse, M. (2015). Suspensions turbulentes de particules de tailles finies: dynamique, modifications de l'écoulement et effets collectifs. Ph.D. thesis, Université de Nice - Sophia Antipolis.
- [18] Clift, R., Grace, J., & Weber, M. (1978). Bubbles, drops and particles. Academic Press.
- [19] Climent, E., & Maxey, M. (2003). Numerical simulations of random suspensions at finite reynolds numbers. *Int. J. Multiphase Flow*, [29\(4\)](#), 579–601.
- [20] Costa, P., Picano, F., Brandt, L., & Breugem, W.-P. (2016). Universal scaling laws for dense particle suspensions in turbulent wall-bounded flows. *Phys. Rev. Lett.*, [117](#), 134501.
- [21] Costa, P., Picano, F., Brandt, L., & Breugem, W.-P. (2018). Effects of the finite particle size in turbulent wall-bounded flows of dense suspensions. *J. Fluid Mech.*, [843](#), 450–478.
- [22] Derksen, J. (2009). Drag on random assemblies of spheres in shear-thinning and thixotropic liquids. *Phys. Fluids*, [21](#), 083302.
- [23] Derksen, J. (2014). Simulations of solid-liquid mass transfer in fixed and fluidized beds. *Chem. Eng. J.*, [255](#), 233—244.
- [24] Derksen, J., & Sundaresan, S. (2007). Direct numerical simulations of dense suspensions: wave instabilities in liquid-fluidized beds. *J. Fluid Mech.*, [587](#), 303–336.
- [25] Derksen, J. J. (2011). Simulations of granular bed erosion due to laminar shear flow near the critical Shields number. *Phys. Fluids*, [23\(11\)](#), 113303.
- [26] Derksen, J. J. (2015). Simulations of granular bed erosion due to a mildly turbulent shear flow. *J. Hydraul. Res.*, [53\(5\)](#), 622–632.
- [27] Derksen, J. J. (2019). Liquid fluidization with cylindrical particles: Highly resolved simulations. *AIChE Journal*, [65\(6\)](#), e16594.
- [28] Doychev, T. (2015). The dynamics of finite-size settling particles. Ph.D. thesis, Karlsruher Institut für Technologie (KIT), KIT Scientific Publishing.
- [29] Duran Vinent, O., Andreotti, B., Claudin, P., & Winter, C. (2019). A unified model of ripples and dunes in water and planetary environments. *Nature Geoscience*, [12\(5\)](#), 345–350.
- [30] Duru, P., Nicolas, M., Hinch, J., & Guazelli, E. (2002). Constitutive laws in liquid-fluidized beds. *J. Fluid Mech.*, [452](#), 371—404.
- [31] Ern, P., Risso, F., Fabre, D., & Magnaudet, J. (2012). Wake-Induced Oscillatory Paths of Bodies Freely Rising or Falling in Fluids. *Annu. Rev. Fluid Mech.*, [44](#), 97–121.

- [32] Eshghinejadfard, A., Hosseini, S., & Thévenin, D. (2019). Effect of particle density in turbulent channel flows with resolved oblate spheroids. *Comput. & Fluids*, [184](#), 29–39.
- [33] Eshghinejadfard, A., Zhao, L., & Thévenin, D. (2018). Lattice Boltzmann simulation of resolved oblate spheroids in wall turbulence. *J. Fluid Mech.*, [849](#), 510–540.
- [34] Esteghamatian, A., & Zaki, T. (2021). The dynamics of settling particles in vertical channel flows: gravity, lift and particle clusters. *J. Fluid Mech.*, [918](#), A33.
- [35] Eswaran, V., & Pope, S. (1988). An examination of forcing in direct numerical simulations of turbulence. *Computers & Fluids*, [16](#), 257–278.
- [36] Fornari, W., Ardekani, M., & Brandt, L. (2018). Clustering and increased settling speed of oblate particles at finite reynolds number. *J. Fluid Mech.*, [848](#), 696–721.
- [37] Fornari, W., Formenti, A., Picano, F., & Brandt, L. (2016). The effect of particle density in turbulent channel flow laden with finite size particles in semi-dilute conditions. *Phys. Fluids*, [28](#)(3), 033301.
- [38] Fornari, W., Kazerooni, H., Hussong, J., & Brandt, L. (2018). Suspensions of finite-size neutrally buoyant spheres in turbulent duct flow. *J. Fluid Mech.*, [851](#), 148–186.
- [39] Fornari, W., Picano, F., & Brandt, L. (2016). Sedimentation of finite-size spheres in quiescent and turbulent environments. *J. Fluid Mech.*, [788](#), 640–669.
- [40] Fornari, W., Picano, F., Sardina, G., & Brandt, L. (2016). Reduced particle settling speed in turbulence. *J. Fluid Mech.*, [808](#), 153–167.
- [41] Fornari, W., Zade, S., Brandt, L., & Picano, F. (2018). Settling of finite-size particles in turbulence at different volume fractions. *Acta Mechanica*, [230](#)(2), 413–430.
- [42] Fröhlich, K., Farmand, P., Pitsch, H., Meinke, M., & Schröder, W. (2021). Particle Reynolds number effects on settling ellipsoids in isotropic turbulence. *International Journal of Multiphase Flow*, [139](#), 103566.
- [43] Fröhlich, K., Meinke, M., & Schröder, W. (2020). Correlations for inclined prolates based on highly resolved simulations. *Journal of Fluid Mechanics*, [901](#), A5.
- [44] Fukuda, T., & Fukuoka, S. (2019). Interface-resolved large eddy simulations of hyperconcentrated flows using spheres and gravel particles. *Advances in Water Resources*, [129](#), 297–310.
- [45] Fukuoka, S., Fukuda, T., & Uchida, T. (2014). Effects of sizes and shapes of gravel particles on sediment transports and bed variations in a numerical movable-bed channel. *Advances in Water Resources*, [72](#), 84–96.
- [46] Gao, X., Yu, J., Lu, L., Li, C., & Rogers, W. A. (2021). Development and validation of SuperDEM-CFD coupled model for simulating non-spherical particles hydrodynamics in fluidized beds. *Chemical Engineering Journal*, [420](#), 127654.
- [47] García, M. H. (2008). Sediment transport and morphodynamics. In M. H. García (Ed.) *Sedimentation Engineering. Processes, Measurements, Modeling and Practice*, (pp. 21–163). American Society of Civil Engineers.

- [48] García-Villalba, M., Kidanemariam, A., & Uhlmann, M. (2012). DNS of vertical plane channel flow with finite-size particles: Voronoi analysis, acceleration statistics and particle-conditioned averaging. *Int. J. Multiphase Flow*, [46](#), 54–74.
- [49] Goto, S., & Vassilicos, J. (2008). Sweep-stick mechanism of heavy particle clustering in fluid turbulence. *Phys. Rev. Lett.*, [100](#)(5), 054503.
- [50] Gupta, A., Clercx, H., & Toschi, F. (2018). Effect of particle shape on fluid statistics and particle dynamics in turbulent pipe flow. *Eur. Phys. J. E*, [41](#)(10), 1–15.
- [51] Hasimoto, H. (1959). On the periodic fundamental solutions of the stokes equations and their application to viscous flow past a cubic array of spheres. *J. Fluid Mech.*, [5](#), 317–328.
- [52] Hölzer, A., & Sommerfeld, M. (2009). Lattice Boltzmann simulations to determine drag, lift and torque acting on non-spherical particles. *Computers & Fluids*, [38](#)(3), 572–589.
- [53] Homann, H., & Bec, J. (2010). Finite-size effects in the dynamics of neutrally buoyant particles in turbulent flow. *J. Fluid Mech.*, [651](#), 81–91.
- [54] Homann, H., Bec, J., & Grauer, R. (2013). Effect of turbulent fluctuations on the drag and lift forces on a towed sphere and its boundary layer. *J. Fluid Mech.*, [721](#), 155–179.
- [55] Huisman, S., Barois, T., Bourgoin, M., Chouippe, A., Doychev, T., Huck, P., Bello Morales, C., Uhlmann, M., & Volk, R. (2016). Columnar structure formation of a dilute suspension of settling spherical particles in a quiescent fluid. *Physical Review Fluids*, [1](#)(7).
- [56] Jain, R., Tschisgale, S., & Fröhlich, J. (2020). Effect of particle shape on bedload sediment transport in case of small particle loading. *Meccanica*, [55](#)(2), 299–315.
- [57] Jain, R., Tschisgale, S., & Fröhlich, J. (2021). Impact of shape: DNS of sediment transport with non-spherical particles. *J. Fluid Mech.*, [916](#).
- [58] Jain, R., Vowinckel, B., & Fröhlich, J. (2017). Spanwise particle clusters in DNS of sediment transport over a regular and an irregular bed. *Flow Turbul Combust*, [99](#)(3-4), 973–990.
- [59] Ji, C., Munjiza, A., Avital, E., Ma, J., & Williams, J. J. R. (2013). Direct numerical simulation of sediment entrainment in turbulent channel flow. *Physics of Fluids*, [25](#)(5), 056601.
- [60] Ji, C., Munjiza, A., Avital, E., Xu, D., & Williams, J. (2014). Saltation of particles in turbulent channel flow. *Physical Review E*, [89](#)(5).
- [61] Jiménez, J. (2004). Turbulent flows over rough walls. *Annu. Rev. Fluid Mech.*, [36](#)(1), 173–196.
- [62] Kaftori, D., Hetsroni, G., & Banerjee, S. (1995). Particle behaviour in the turbulent boundary layer. I. Motion, deposition, and entrainment. *Phys. Fluids*, [7](#)(5), 1095 – 1107.
- [63] Kajishima, T. (2004). Influence of particle rotation on the interaction between particle clusters and particle-induced turbulence. *Int. J. Heat Fluid Flow*, [25](#)(5), 721–728.
- [64] Kajishima, T., & Takiguchi, S. (2002). Interaction between particle clusters and particle-induced turbulence. *Int. J. Heat Fluid Flow*, [23](#), 639–646.

- [65] Kajishima, T., Takiguchi, S., Hamasaki, H., & Miyake, Y. (2001). Turbulence structure of particle-laden flow in a vertical plane channel due to vortex shedding. *JSME Int. J., Series B*, [44\(4\)](#), 526–535.
- [66] Kawahara, G., Uhlmann, M., & van Veen, L. (2012). The significance of simple invariant solutions in turbulent flows. *Ann. Rev. Fluid Mech.*, [44](#), 203–225.
- [67] Kharrouba, M., Pierson, J.-L., & Magnaudet, J. (2021). Flow structure and loads over inclined cylindrical rodlike particles and fibers. *Physical Review Fluids*, [6\(4\)](#), 044308.
- [68] Kidanemariam, A. G. (2015). *The formation of patterns in subaqueous sediment*. Ph.D. thesis, Karlsruhe Institute of Technology.
- [69] Kidanemariam, A. G., Chan-Braun, C., Doychev, T., & Uhlmann, M. (2013). Direct numerical simulation of horizontal open channel flow with finite-size, heavy particles at low solid volume fraction. *New J. Phys.*, [15\(2\)](#), 025031.
- [70] Kidanemariam, A. G., Scherer, M., & Uhlmann, M. (2022). Open channel flow over evolving subaqueous ripples. *J. Fluid Mech.*, [937](#), A26.
- [71] Kidanemariam, A. G., & Uhlmann, M. (2014). Direct numerical simulation of pattern formation in subaqueous sediment. *J. Fluid Mech.*, [750](#), R2.
- [72] Kidanemariam, A. G., & Uhlmann, M. (2014). Interface-resolved direct numerical simulation of the erosion of a sediment bed sheared by laminar channel flow. *Int. J. Multiph. Flow*, [67](#), 174–188.
- [73] Kidanemariam, A. G., & Uhlmann, M. (2017). Formation of sediment patterns in channel flow: minimal unstable systems and their temporal evolution. *J. Fluid Mech.*, [818](#), 716–743.
- [74] Ladd, A. (1994). Numerical simulations of particulate suspensions via a discretized boltzmann equation. part 2. numerical results. *J. Fluid Mech.*, [271](#), 311–339.
- [75] Lashgari, I., Picano, F., Breugem, W.-P., & Brandt, L. (2014). Laminar, turbulent, and inertial shear-thickening regimes in channel flow of neutrally buoyant particle suspensions. *Phys. Rev. Lett.*, [113](#), 254502.
- [76] Lashgari, I., Picano, F., Costa, P., Breugem, W.-P., & Brandt, L. (2017). Turbulent channel flow of a dense binary mixture of rigid particles. *J. Fluid Mech.*, [818](#), 623–645.
- [77] Lee, H., & Balachandar, S. (2010). Drag and lift forces on a spherical particle moving on a wall in a shear flow at finite  $Re$ . *J. Fluid Mech.*, [657](#), 89–125.
- [78] Li, X., Jiang, M., Huang, Z., & Zhou, Q. (2021). Effect of particle orientation on the drag force in random arrays of oblate ellipsoids in low-Reynolds-number flows. *AIChE Journal*, [67\(1\)](#), e17040.
- [79] Loisel, V., Abbas, M., Masbernat, O., & Climent, E. (2013). The effect of neutrally buoyant finite-size particles on channel flows in the laminar-turbulent transition regime. *Phys. Fluids*, [25\(12\)](#), 123304.
- [80] Lucci, F., Ferrante, A., & Elghobashi, S. (2010). Modulation of isotropic turbulence by particles of taylor length-scale size. *J. Fluid Mech.*, [650](#), 5–55.

- [81] Matas, J.-P., Morris, J., & Guazzelli, E. (2003). Transition to turbulence in particulate pipe flow. *Phys. Rev. Lett.*, 90(1), 014501.
- [82] Maxey, M. (1987). The gravitational settling of aerosol particles in homogeneous turbulence and random flow fields. *J. Fluid Mech.*, 174, 441–465.
- [83] Mazzuoli, M., Kidanemariam, A. G., & Uhlmann, M. (2019). Direct numerical simulations of ripples in an oscillatory flow. *J. Fluid Mech.*, 863, 572–600.
- [84] Mehrabadi, M., Murphy, E., & Subramaniam, S. (2016). Development of a gas–solid drag law for clustered particles using particle-resolved direct numerical simulation. *Chem. Eng. Sci.*, 152, 199–212.
- [85] Mehrabadi, M., Tenneti, S., Garg, R., & Subramaniam, S. (2015). Pseudo-turbulent gas-phase velocity fluctuations in homogeneous gas-solid flow: fixed particle assemblies and freely evolving suspensions. *J. Fluid Mech.*, 770, 210–246.
- [86] Mei, R., Adrian, R., & Hanratty, T. (1997). Turbulent Dispersion of Heavy Particles With Nonlinear Drag. *J. Fluids Eng.*, 119(1), 170–179.
- [87] Meng, Q., An, H., Cheng, L., & Kimiaei, M. (2021). Wake transitions behind a cube at low and moderate Reynolds numbers. *Journal of Fluid Mechanics*, 919, A44–37.
- [88] Meyer-Peter, E., & Müller, R. (1948). Formulas for bed-load transport. In IAHR (Ed.) *Proc. 2nd Meet.*, (pp. 39–64). Stockholm, Sweden.
- [89] Moin, P., & Mahesh, K. (1998). Direct numerical simulation: A tool in turbulence research. *Annu. Rev. Fluid Mech.*, 30, 539–578.
- [90] Monchaux, R., Bourgoin, M., & Cartellier, a. (2010). Preferential concentration of heavy particles: A Voronoï analysis. *Phys. Fluids*, 22(10), 103304.
- [91] Mordant, N., Crawford, A., & Bodenschatz, E. (2004). Three-dimensional structure of the lagrangian acceleration in turbulent flows. *Phy. Rev. Lett.*, 93(21).
- [92] Moriche, M., Uhlmann, M., & Dušek, J. (2021). A single oblate spheroid settling in unbounded ambient fluid: A benchmark for simulations in steady and unsteady wake regimes. *International Journal of Multiphase Flow*, 136, 103519.
- [93] Munjiza, A., & Andrews, K. R. F. (2000). Penalty function method for combined finite-discrete element systems comprising large number of separate bodies. *International Journal for Numerical Methods in Engineering*, 49(11), 1377–1396.
- [94] Niazi Ardekani, M., & Brandt, L. (2019). Turbulence modulation in channel flow of finite-size spheroidal particles. *Journal of Fluid Mechanics*, 859, 887–901.
- [95] Nicolai, H., Herzhaft, B., Hinch, E., Oger, L., & Guazzelli, E. (1995). Particle velocity fluctuations and hydrodynamic self-diffusion of sedimenting non-brownian spheres. *Physics of Fluids*, 7(1), 12–23.
- [96] Niño, Y., & García, M. H. (1996). Experiments on particle-turbulence interactions in the near-wall region of an open channel flow: implications for sediment transport. *J. Fluid Mech.*, 326, 285–319.



- [97] Ouriemi, M., Aussillous, P., Medale, M., Peysson, Y., & Guazzelli, É. (2007). Determination of the critical shields number for particle erosion in laminar flow. *Phys. Fluids*, [19\(6\)](#), 061706.
- [98] Pestana, T., Uhlmann, M., & Kawahara, G. (2020). Can preferential concentration of finite-size particles in plane Couette turbulence be reproduced with the aid of equilibrium solutions? *Phys. Rev. Fluids*, [5](#), 034305.
- [99] Picano, F., Breugem, W.-P., & Brandt, L. (2015). Turbulent channel flow of dense suspensions of neutrally buoyant spheres. *J. Fluid Mech.*, [764](#), 463–487.
- [100] Pierson, J.-L., Auguste, F., Hammouti, A., & Wachs, A. (2019). Inertial flow past a finite-length axisymmetric cylinder of aspect ratio 3: Effect of the yaw angle. *Physical Review Fluids*, [4\(4\)](#), 044802.
- [101] Qureshi, N. M., Bourgoïn, M., Baudet, C., Cartellier, A., & Gagne, Y. (2007). Turbulent transport of material particles: An experimental study of finite size effects. *Phys. Rev. Lett.*, [99\(November\)](#), 1–4.
- [102] Rahmani, M., Hammouti, A., & Wachs, A. (2018). Momentum balance and stresses in a suspension of spherical particles in a plane Couette flow. *Physics of Fluids*, [30\(4\)](#), 043301.
- [103] Rahmani, M., & Wachs, A. (2014). Free falling and rising of spherical and angular particles. *Physics of Fluids*, [26](#), 083301.
- [104] Reeks, M. (1983). The transport of discrete particles in inhomogeneous turbulence. *J. Aerosol Sci.*, [14\(6\)](#), 729–739.
- [105] Riboux, G., Risso, F., & Legendre, D. (2009). Experimental characterization of the agitation generated by bubbles rising at high reynolds number. *J. Fluid. Mech.*, [643](#), 509–539.
- [106] Richardson, J., & Zaki, W. (1997). Sedimentation and fluidisation: Part i. *Chemical Engineering Research and Design*, [75](#), S82–S100.
- [107] Richter, A., & Nikrityuk, P. (2012). Drag forces and heat transfer coefficients for spherical, cuboidal and ellipsoidal particles in cross flow at sub-critical Reynolds numbers. *International Journal of Heat and Mass Transfer*, [55\(4\)](#), 1343–1354.
- [108] Richter, A., & Nikrityuk, P. (2013). New correlations for heat and fluid flow past ellipsoidal and cubic particles at different angles of attack. *Powder technology*, [249](#), 463–474.
- [109] Risso, F. (2011). Theoretical model for  $k^{-3}$  spectra in dispersed multiphase flows. *Phys. Fluids*, [23\(1\)](#), 011701.
- [110] Rubinstein, G., Derksen, J., & Sundaresan, S. (2016). Lattice boltzmann simulations of low-reynolds-number flow past fluidized spheres: effect of stokes number on drag force. *J. Fluid Mech.*, [788](#), 576–601.
- [111] Saha, A. (2004). Three-dimensional numerical simulations of the transition of flow past a cube. *Physics of Fluids*, [16\(5\)](#), 1630–1646.
- [112] Sangani, A., & Acrivos, A. (1982). Slow flow through a periodic array of spheres. *Int. J. Multiphase Flow*, [4](#), 343–360.

- [113] Sanjeevi, S. K. P., & Padding, J. T. (2017). On the orientational dependence of drag experienced by spheroids. *Journal of Fluid Mechanics*, 820.
- [114] Sanjeevi, S. K. P., & Padding, J. T. (2020). Hydrodynamic forces on monodisperse assemblies of axisymmetric elongated particles: Orientation and voidage effects. *AIChE Journal*, 66(6), e16951.
- [115] Scherer, M., Kidanemariam, A. G., & Uhlmann, M. (2020). On the scaling of the instability of a flat sediment bed with respect to ripple-like patterns. *J. Fluid Mech.*, 900, A1.
- [116] Scherer, M., Uhlmann, M., Kidanemariam, A. G., & Kraymer, M. (2022). On the role of turbulent streaks in generating sediment ridges. *J. Fluid Mech.*, 930, A11.
- [117] Schneiders, L., Meinke, M., & Schröder, W. (2017). Direct particle fluid simulation of Kolmogorov-length-scale size particles in decaying isotropic turbulence. *J. Fluid Mech.*, 819, 188–227.
- [118] Seyed-Ahmadi, A., & Wachs, A. (2019). Dynamics and wakes of freely settling and rising cubes. *Physical Review Fluids*, 4(7), 074304.
- [119] Seyed-Ahmadi, A., & Wachs, A. (2021). Sedimentation of inertial monodisperse suspensions of cubes and spheres. *Phys. Rev. Fluids*, 6(4).
- [120] Shao, X., Wu, T., & Yu, Z. (2012). Fully resolved numerical simulation of particle-laden turbulent flow in a horizontal channel at a low Reynolds number. *J. Fluid Mech.*, 693(1989), 319–344.
- [121] Shields, A. (1936). *Anwendung der Ähnlichkeitsmechanik und der Turbulenzforschung auf die Geschiebetransporte*. Mitteilungen der Versuchsanstalt für Wasserbau und Schiffbau, Technische Hochschule Berlin.
- [122] Soulsby, R., & Whitehouse, R. (1997). Threshold of sediment motion in coastal environments. In *Proceedings of the 13th Australasian Coastal and Ocean Engineering Conference*, (pp. 149–154). Centre for Advanced Engineering, University of Canterbury.
- [123] Tavanashad, V., Passalacqua, A., & Subramaniam, S. (2021). Particle-resolved simulation of freely evolving particle suspensions: Flow physics and modelling. *Int. J. Multiphase Flow*, 135, 103533.
- [124] Tavassoli, H., Peters, E., & Kuipers, J. (2015). Direct numerical simulation of fluid–particle heat transfer in fixed random arrays of non-spherical particles. *Chemical Engineering Science*, 129, 42–48.
- [125] ten Cate, A., Derksen, J., Portela, L., & van den Akker, H. (1994). Fully resolved simulations of colliding spheres in forces isotropic turbulence. *J. Fluid Mech.*, 519, 233–271.
- [126] Tenneti, S., & Subramaniam, S. (2014). Particle-resolved direct numerical simulation for gas-solid flow model development. *Ann. Rev. Fluid Mech.*, 46, 199–230.
- [127] Torquato, S., Truskett, T., & Debenedetti, P. (2000). Is random close packing of spheres well defined? *Phys. Rev. Lett*, 84, 2064–2067.
- [128] Uhlmann, M. (2008). Interface-resolved direct numerical simulation of vertical particulate channel flow in the turbulent regime. *Phys. Fluids*, 20(5), 053305.

- [129] Uhlmann, M. (2020). Voronoï tessellation analysis of sets of randomly placed finite-size spheres. *Physica A: Statistical Mechanics and its Applications*, [555](#), 124618.
- [130] Uhlmann, M., & Chouippe, A. (2017). Clustering and preferential concentration of finite-size particles in forced homogeneous-isotropic turbulence. *J. Fluid Mech.*, [812](#), 991–1023.
- [131] Uhlmann, M., & Doychev, T. (2014). Sedimentation of a dilute suspension of rigid spheres at intermediate Galileo numbers: the effect of clustering upon the particle motion. *J. Fluid Mech.*, [752](#), 310–348.
- [132] Vakil, A., & Green, S. I. (2009). Drag and lift coefficients of inclined finite circular cylinders at moderate Reynolds numbers. *Computers & Fluids*, [38](#)(9), 1771–1781.
- [133] van der Hoef, M., Beetstra, R., & Kuipers, J. (1994). Lattice boltzmann simulations of low reynolds-number flow past mono-and bidisperse arrays of spheres: results for the permeability and drag force. *J. Fluid Mech.*, [528](#), 233–254.
- [134] Volk, R., Calzavarini, E., L  v  que, E., & Pinton, J. (2011). Dynamics of inertial particles in a turbulent von k  rm  n flow. *J. Fluid Mech.*, [668](#), 223–235.
- [135] Vollmari, K., Jasevi  cius, R., & Kruggel-Emden, H. (2016). Experimental and numerical study of fluidization and pressure drop of spherical and non-spherical particles in a model scale fluidized bed. *Powder Technology*, [291](#), 506–521.
- [136] Voth, G., La Porta, A., Crawford, A., Alexander, J., & Bodenschatz, E. (2002). Measurement of particle accelerations in fully developed turbulence. *J. Fluid Mech.*, [469](#), 121–160.
- [137] Vowinckel, B., Biegert, E., Meiburg, E., Aussillous, P., & Guazzelli,   . (2021). Rheology of mobile sediment beds sheared by viscous, pressure-driven flows. *J. Fluid Mech.*, [921](#).
- [138] Vowinckel, B., Jain, R., Kempe, T., & Fr  hlich, J. (2016). Entrainment of single particles in a turbulent open-channel flow: a numerical study. *J. Hydraul. Res.*, [54](#)(2), 158–171.
- [139] Vowinckel, B., Kempe, T., & Fr  hlich, J. (2014). Fluid-particle interaction in turbulent open channel flow with fully-resolved mobile beds. *Adv. Water Resour.*, [72](#), 32–44.
- [140] Vowinckel, B., Nikora, V., Kempe, T., & Fr  hlich, J. (2017). Momentum balance in flows over mobile granular beds: application of double-averaging methodology to DNS data. *J. Hydraul. Res.*, [55](#)(2), 190–207.
- [141] Vowinckel, B., Nikora, V., Kempe, T., & Fr  hlich, J. (2017). Spatially-averaged momentum fluxes and stresses in flows over mobile granular beds: a DNS-based study. *J. Hydraul. Res.*, [55](#)(2), 208–223.
- [142] Wang, G., Abbas, M., & Climent, E. (2017). Modulation of large-scale structures by neutrally buoyant and inertial finite-size particles in turbulent Couette flow. *Phys. Rev. Fluids*, [2](#), 084302.
- [143] Wen, C., & Yu, Y. (1966). Mechanics of fluidization. *Chem. Engng Prog.*, [62](#), 100–111.
- [144] Wong, M., & Parker, G. (2006). Reanalysis and Correction of Bed-Load Relation of Meyer-Peter and M  ller Using Their Own Database. *J. Hydraul. Eng.*, [132](#), 1159–1168.

- [145] Yeo, K., Dong, S., Climent, E., & Maxey, M. (2010). Modulation of homogeneous turbulence seeded with finite size bubbles or particles. International Journal of Multiphase Flow, [36\(3\)](#), [221–233](#).
- [146] Yousefi, A., Costa, P., & Brandt, L. (2020). Single sediment dynamics in turbulent flow over a porous bed – insights from interface-resolved simulations. Journal of Fluid Mechanics, [893](#).
- [147] Yu, W., Vinkovic, I., & Buffat, M. (2016). Acceleration statistics of finite-size particles in turbulent channel flow in the absence of gravity. Flow, Turbulence and Combustion, [96\(1\)](#), [183–205](#).
- [148] Yu, Z., Lin, Z., Shao, X., & Wang, L.-P. (2017). Effects of particle-fluid density ratio on the interactions between the turbulent channel flow and finite-size particles. Phys. Rev. E, [96](#), [033102](#).
- [149] Yu, Z., Wu, T., Shao, X., & Lin, J. (2013). Numerical studies of the effects of large neutrally buoyant particles on the flow instability and transition to turbulence in pipe flow. Phys. Fluids, [25\(4\)](#), 043305.
- [150] Yu, Z., Xia, Y., Guo, Y., & Lin, J. (2021). Modulation of turbulence intensity by heavy finite-size particles in upward channel flow. J. Fluid Mech., [913](#), [A3](#).
- [151] Zade, S., Fornari, W., Lundell, F., & Brandt, L. (2019). Buoyant finite-size particles in turbulent duct flow. Phys. Rev. Fluids, [4](#), [024303](#).
- [152] Zaidi, A., Tsuji, T., & Tanaka, T. (2014). Direct numerical simulation of finite sized particles settling for high reynolds number and dilute suspension. Int. J. Heat Fluid Flow, [50](#), 330–341.
- [153] Zastawny, M., Mallouppas, G., Zhao, F., & Van Wachem, B. (2012). Derivation of drag and lift force and torque coefficients for non-spherical particles in flows. International Journal of Multiphase Flow, [39](#), 227–239.
- [154] Zeng, L., Balachandar, S., & Fischer, P. (2005). Wall-induced forces on a rigid sphere at finite Reynolds numbers. J. Fluid Mech., [536](#), 1–25.
- [155] Zhang, B., Xu, D., Zhang, B., Ji, C., Munjiza, A., & Williams, J. (2020). Numerical investigation on the incipient motion of non-spherical sediment particles in bedload regime of open channel flows. Computational Particle Mechanics, [7\(5\)](#), [987–1003](#).
- [156] Zhu, C., Yu, Z., Pan, D., & Shao, X. (2020). Interface-resolved direct numerical simulations of the interactions between spheroidal particles and upward vertical turbulent channel flows. J. Fluid Mech., [891](#), [A6](#).
- [157] Zhu, C., Yu, Z., & Shao, X. (2018). Interface-resolved direct numerical simulations of the interactions between neutrally buoyant spheroidal particles and turbulent channel flows. Phys. Fluids, [30\(11\)](#), [115103](#).